Modelling of Halo and Tail Generation in Electron Beams

Modellierung haloformierender Prozesse in Elektronenstrahlen

Diplomarbeit im Fach Physik

vorgelegt von
cand. phys. Miriam Fitterer

Hauptreferent: Prof. Dr. T. Baumbach
Laboratorium für Applikationen der Synchrotronstrahlung
der Universität Karlsruhe (TH)

Koreferent: Prof. Dr. G. Quast
Institut fr Experimentelle Kernphysik
der Universität Karlsruhe (TH)

Oktober 2009

Hiermit erkläre ich, dass ich die vorliegende Arbeit selbstständig angefertigt und keine anderen als die angegebenen Quellen und Hilfsmittel verwendet habe.

Karlsruhe, den 25. September 2008

Miriam Fitterer

Als Diplomarbeit akzeptiert:

Contents

Chapter 1

Linear Accelerators

The research of particle physics demands high beam energies and luminosity. Circular accelerators are generally more economic than linear accelerators, because the beam circulates many times until it is finally dumped. The disadvantage is that the energy loss due to synchrotron radiation increases considerably with rising beam energy. In linear accelerators this effect is negligible (ch. 1.4). Other advantages of linear accelerators are the relatively easy focusing resulting in a small beam size and a low energy spread, the absence of multiturn effects and an easier injection and extraction of the beam. Future high energy high luminosity accelerators therefore focus on the concept of linear acceleration.

1.1 Layout of Linear e^+e^- - Accelerators

Linear accelerators consist of three basic units, the *source*, the *injector* and the *main accelerator*.

Electrons can be generated by a *thermionic gun*, where a heated cathode of a special material emits electrons, or a photo cathode, where a strong laser pulse knocks out electrons of a cathode. Devices where an accelerating rf cavity follows the photo cathode are called *rf guns*.

Positrons are created by aiming a relatively high energy electron beam on a heavy metal target, where by electromagnetic pair production, positrons are created. The positrons and electrons are then separated by strong electromagnetic fields.

Particles are commonly accelerated with rf fields, which require a specific time structure of the beam. If a photo cathode is used the time structure can be created by pulsing the laser in the right way. In the case of a thermionic gun, a chopper and a prebuncher must be used. For positrons the desired time structure is provided by giving the generating electron beam the right time structure. As the source already gives the beam its time structure, it builds the basis for the further behaviour of the beam and has a great influence on the beam dynamics throughout the whole accelerator. A careful choice of the source is therefore essential.

The positron beam produced by the source normally has a too large beam size and beam divergence to be directly accelerated in the main linac. Both are reduced in so called *damping rings*, where the particles simply circulate for some time without being accelerated. The principle of damping rings is, that the particles lose their transverse momenta through the emission of synchrotron radiation photons. To reduce the damping time and achieve the required beam sizes for further acceleration, damping wigglers are used in addition or instead. They consist of alternating dipoles, which force the particles on a sinusoidal trajectory. As the bending radius is very small and the number of bends is high, the particles strongly emit synchrotron radiation and the transverse oscillations are damped fast. Damping rings are also used for electrons if needed. After the damping rings the particles are transfered directly or via a transfer line to the main accelerator. A typical layout of a linear accelerator is the CLIC layout (fig. 2.0.1)

1.2 Beam Dynamics

In every accelerator the particles are supposed to follow a determinate path. For the description of the particle trajectories a specific coordinate system is used, where the coordinates are separated into two different parts (fig. 1.2.1). One part describes the ideal path or *reference path* through the beamline and the other part the offset from it.

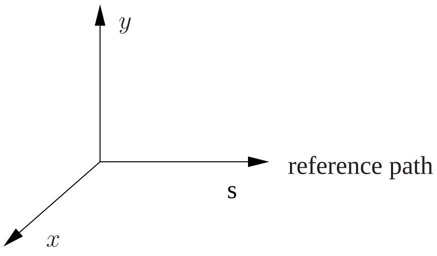

Figure 1.2.1: Coordinate system

To keep the beam close to the ideal path throughout the lattice and accelerate it to the desired energy, electromagnetic fields are used. Their effect on one particle with charge q and velocity $\vec{v}$ is given by the Lorentz force:

$$\vec{F} = q(\vec{E} + \vec{v} \times \vec{B}) \tag{1.2.1}$$

For relativistic particles the force from a magnetic field of $1\ \mathrm{T}$ is equivalent to the one of an electric field of $3 \times 10^8\ \mathrm{V/m}$. A magnetic field of $1\ \mathrm{T}$ can be easily generated, but a field of $3 \times 10^8\ \mathrm{V/m}$ is impossible to reach. Therefore rf electromagnetic fields are used for particle acceleration (ch. 1.2.1) and magnetic fields for particle guidance (ch. 1.2.2).

1.2.1 RF Acceleration

In the very beginning of accelerator physics, the particles were accelerated with electrostatic fields. These were limited by electrical breakdown. In 1925 Ising proposed to accelerate the particles with high frequency alternating fields. Nowadays most accelerators use radio frequency (rf) cavities, which are excited by rf generators like klystrons.
Simplified the electromagnetic field seen by the beam in a cavity has a sinusoidal shape. During the half period, when the field is positive, the particles are accelerated, while during the other half period, the beam must be shielded from the field in order not to be decelerated. Technically this is realized by inserting metallic drift tubes. The length of the tube segments are chosen such that the particles reach the gap between two successive tubes at the moment the rf field is accelerating.
Each cavity is designed to produce a given energy gain per cell. Particles with the correct initial velocity then gain the right amount of energy and maintain synchronism with the accelerating field. There are two phases where the energy gain per cell is equal to the design value. Only the earlier phase is called the *synchronous phase* and leads to a stable orbit. Particles that arrive earlier than the synchronous phase, so particles with too much energy, experience a smaller accelerating field, and particles that arrive later, so particles with too little energy, will experience a larger field (fig. 1.2.2). Driven by this mechanism the particles will start to oscillate around the synchronous phase. As the particles approach relativistic energies, the phase oscillations slow down, and the particles maintain an almost constant phase relative to the traveling wave.

1.2.2 Linear Beam Dynamics

For the beam transport through the whole accelerator electromagnet fields are used. Because the transverse beam size is normally very small, it is useful to expand the magnetic field around the reference orbit.

$$\begin{aligned}
\frac{q}{p}B_z(x) &= \frac{q}{p}B_{z0} + \frac{q}{p}\frac{dB_z}{dx}x + \frac{1}{2!}\frac{q}{p}\frac{d^2B_z}{dx^2}x^2 + \frac{1}{3!}\frac{q}{p}\frac{d^3B_z}{dx^3}x^3 + \cdots \\
&= \frac{1}{R} + kx + \frac{1}{2!}mx^2 + \frac{1}{3!}ox^3 + \cdots \\
& \text{Dipol} \quad \text{Quadrupol} \quad \text{Sextupol} \quad \text{Oktupol} + \cdots
\end{aligned} \tag{1.2.2}$$

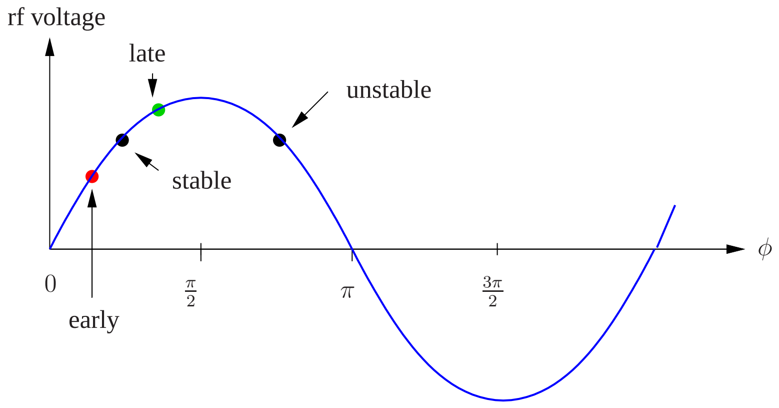

Figure 1.2.2: Schematic drawing of an rf wave: a stable operation requires that $0 < \phi < \pi/2$.

As shown the field can be split up in a sum of multipoles, where each multipole has a different effect on the particles. Dipoles bend the orbit, quadrupoles focus the beam, sextupoles compensate chromatic effects and octupoles correct the influence of field errors. The part of beam dynamics including only lattices with dipoles and quadrupoles, so linear magnetic fields, is called *linear beam dynamics*.

Transverse Focusing by Magnetic Quadrupoles

Focusing is needed in a linear accelerator, because the particles are commonly defocused by the rf transverse electric fields. In addition the beam size increases, because the initial beam particles always have finite non zero transverse velocity and are repelled by each other due to the Coulomb forces. Therefore transverse focusing is needed to ensure a stable operation. The most common solution is to include magnetic-quadrupole focusing lenses.

A quadrupole is suited for focusing because the field increases linearly from the center and particles with a larger offset to the ideal orbit experience a stronger focusing force than particles with a smaller offset which leads to an overall focusing of the beam (fig. 1.2.3). The field pattern of a quadrupole shows, that the particles are only focused in one plane and are defocused in the other plane (fig. 1.2.3). A total focusing of the beam in both transverse planes can be obtained by a combination of quadrupoles. The most common arrangement is a FODO cell (fig. 1.2.4). FODO stands for the order of the elements: Focusing quadrupole, drift length, Defocusing quadrupole, drift length. The drift lengths are often substituted by other elements like accelerating structures, beam position monitors etc.

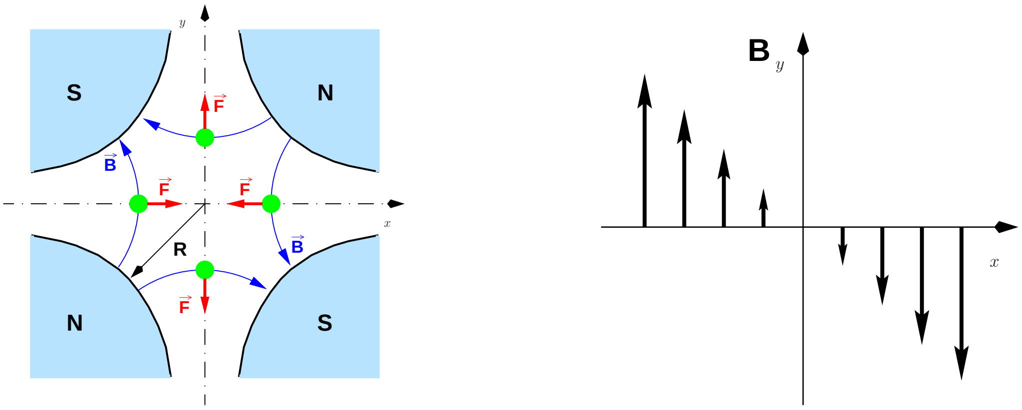

Figure 1.2.3: Field of magnetic Quadrupole: The Quadrupole has a focusing effect in the x-plane and a defocusing effect in the y-plane. The field strength increases linearly from the center.

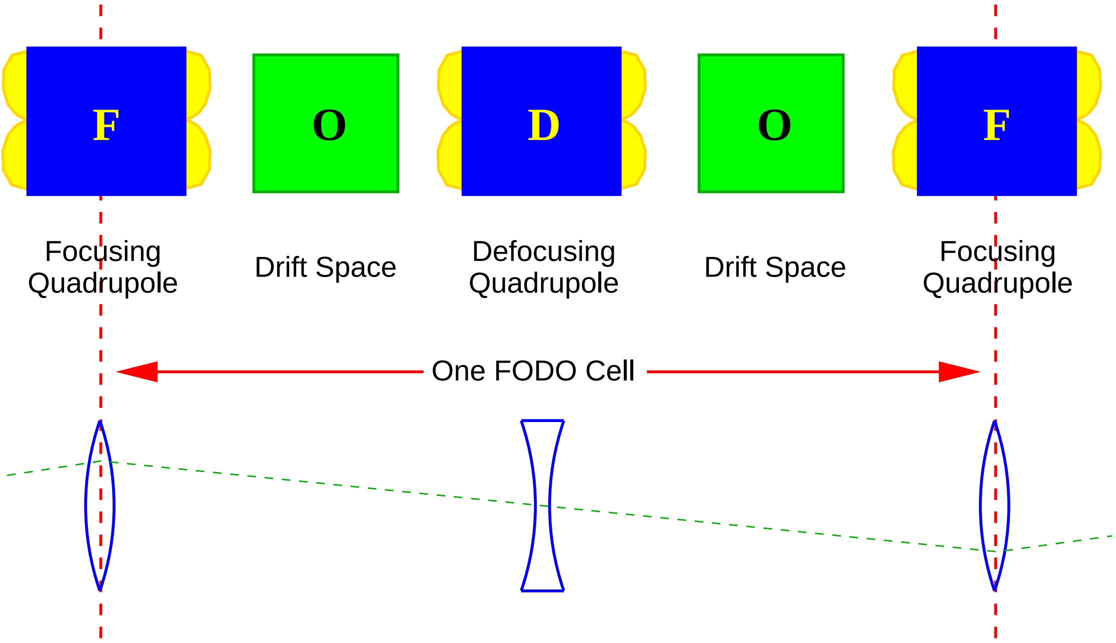

Figure 1.2.4: FODO lattice: The combination of a focusing magnetic-quadrupole lens and a following defocusing magnetic-quadrupole lens, results in an overall focus of the beam particles as known from classical optics. The focusing and defocusing quadrupole have the same focal strength $\frac{1}{f} = kl$ and the distance between two equal lenses is 2f.

Equation of Motion and Matrix formalism

In linear beam dynamics the two transverse coordinates are decoupled from each other and it is sufficient to treat one of them. As bending magnets are only needed in linear accelerators for transfer lines or damping rings and the main interest lies in the main accelerator, this chapter will treat only lattices consisting of quadrupoles and drifts.

The particle trajectory in a sequence of quadrupoles is described by the *Hill's equation of motion*:

$$x'' + k(s)x = 0 \tag{1.2.3}$$

where x'' is a acronym for $\frac{d^2x}{ds^2}$ and $k(s)$ the quadrupole strength defined in eq. (1.2.2). A quadrupole has a focusing effect if $k > 0$ and a defocusing one if $k < 0$. Because eq. (1.2.3) is a linear second-order differential equation, its solution can be written in matrix form:

$$\begin{pmatrix} x \\ x' \end{pmatrix} = \begin{pmatrix} a & b \\ c & d \end{pmatrix} \begin{pmatrix} x_0 \\ x'_0 \end{pmatrix} \tag{1.2.4}$$

where x_0 and x'_0 are the initial displacement and divergence angle and x and x' are the final values. The 2×2 matrix is called *transfer matrix*. The total transfer matrix through a sequence of elements is obtained by forming the product of the individual transfer matrices. If the beam passes the elements $1,\ 2,\ 3,\ \cdots,\ n$ the total transfer matrix is $R = R_n \cdot \cdots \cdot R_3 \cdot R_2 \cdot R_1$.

Twiss Parameters

If $k(s)$ is a periodic function of s the solution of Hill's equation has a form similar to that of a harmonic oscillator:

$$x(s) = \sqrt{\epsilon\beta(s)} \cos\left(\phi(s) + \phi_0\right) \tag{1.2.5}$$

ϵ and ϕ_0 are constants determined by the initial conditions. $\beta(s)$ and $\phi(s)$ are called amplitude and phase function and are related by:

$$\phi(s) = \int_0^s \frac{1}{\beta(\tilde{s})} d\tilde{s} \tag{1.2.6}$$

It can be shown that x and x' satisfy the equation:

$$\gamma(s)x^2 + 2\alpha(s)xx' + \beta(s)x'^2 = \epsilon \tag{1.2.7}$$

where $\gamma\beta - \alpha^2 = 1$. Eq. (1.2.7) is the general equation of an ellipse with the center at the origin of the x-x' phase space and area $\pi\epsilon$ (fig. 1.2.5). The parameters $\gamma(s)$, $\alpha(s)$ and $\beta(s)$ describing the ellipse are called *twiss parameters* and are all periodic functions of s with the same period as $k(s)$. ϵ is the *emittance*.

In chapter 1.2.2 the matrix formalism to transport particle coordinates between two points of the lattice has been introduced. This formalism can be also applied to the beam ellipse. Instead of transforming single particle coordinates, the whole ellipse, defined by the *twiss matrix*:

$$\sigma = \begin{pmatrix} \beta & -\alpha \\ -\alpha & \gamma \end{pmatrix} \tag{1.2.8}$$

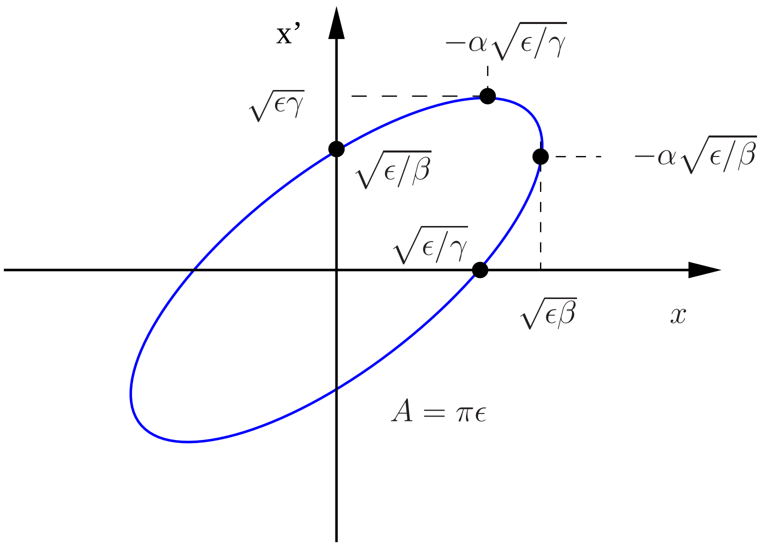

Figure 1.2.5: Phase space ellipse

is transformed. Equation (1.2.7) is equivalent to the matrix form $X^\top \sigma^{-1} X = \epsilon$, where $X = (x_0, x_0')^\top$ are the phase space coordinates. If R is the transfer matrix between the initial phase space coordinates X_0 and the final phase space coordinates X, than the initial twiss matrix σ_0 transforms like:

$$\sigma = R \sigma_0 R^\top \tag{1.2.9}$$

It is important to note, that because all transformations are linear, the beam emittance ϵ stays constant.

Beam Matrix

In linear accelerators the phase-space beam distribution has often an elliptical shape, because linear forces dominate the beam dynamics. To estimate the transformation of the beam through the lattice, the phase-space beam distribution can be enclosed by an ellipse in phase space. The general equation for an ellipse is given by equation (1.2.7), which is also used for the description of the beam ellipse. Because beam distributions typically have gaussian shape and thus no sharp contours, it is useful to work with the rms-values of the distribution. The ellipse parameters β and γ are defined such that the ellipse projection on the x-x' axes equals the rms values of the distribution. α is defined, so that the rms ellipse coincides with the trajectory ellipse. This definition yields:

$$\begin{aligned} \sigma_x^2 &= \overline{x^2} = \sqrt{\beta\epsilon} \\ \sigma_{x'}^2 &= \overline{x'^2} = \sqrt{\gamma\epsilon} \\ \sigma_{xx'} &= \overline{xx'} = -\alpha\epsilon \end{aligned} \tag{1.2.10}$$

σ_x is called the *beam envelope* and σ'_x the *beam divergence*. The emittance is then given by:

$$\epsilon = \sqrt{\sigma_x^2 \sigma_{x'}^2 - \sigma_{xx'}^2} \tag{1.2.11}$$

Analogical to the twiss matrix, the beam matrix is defined by:

$$\sigma = \begin{pmatrix} \sigma_x^2 & \sigma_{xx'} \\ \sigma_{xx'} & \sigma_{x'}^2 \end{pmatrix} \tag{1.2.12}$$

and is related to the twiss matrix by $\sigma_{\text{Beam}} = \epsilon \sigma_{\text{Twiss}}$.
The emittance defined by eq. (1.2.11) is conserved under two conditions: that Liouville's theorem is satisfied in the six-dimensional phase space and that the forces are uncoupled in the three directions. If acceleration and deceleration of the beam are allowed, the rms emittance doesn't stay constant any more. Applying Liouville's theorem again, one finds that the so called normalized emittance defined by

$$\epsilon_{\text{normalized}} = \beta\gamma\epsilon_{\text{rms}} \tag{1.2.13}$$

is conserved. In this case $\gamma = E/mc^2$ is the relativistic γ-factor and β the velocity in units of the speed of light.

1.2.3 Dispersion

Particles beams are in general not monoenergetic but have a very small finite energy or momentum spread $\Delta p/p$. The effect of the momentum offset on the particle trajectory can be best described with the dispersion function, which is defined as the trajectory of a particle with $\Delta p/p = 1$. The transverse position $x_{\text{tot}}(s)$ of a particle with momentum offset $\Delta p/p$ is then given by [1]:

$$x_{\text{tot}}(s) = x(s) + D(s)\frac{\Delta p}{p} \tag{1.2.14}$$

where $x(s)$ is the trajectory of the reference particle with $\Delta p/p = 0)$.

1.3 Basics of RF Cavities

In this chapter we only give a short summary of the basics of rf cavities using the example of a cylindrical cavity and focus on the subjects relevant for the CLIC accelerating and decelerating structures as well as for the TESLA cavities. Accelerating structures in general are discussed in [2] and [3]. A list of the characterizing parameters is given in A.

1.3.1 Cylindrical Cavity

Particles are commonly accelerated by high frequency alternating fields (ch. 1.2.1). Free electromagnetic waves do not have a component in the longitudinal direction and are therefore not usable without modification. By introducing the right boundary conditions electromagnetic waves obtain a longitudinal field component, which is given by the Laplace equation:

$$\nabla^2 \vec{E} - \frac{1}{c^2} \frac{\partial^2 \vec{E}}{\partial t^2} \tag{1.3.1}$$

with the solution for the longitudinal component:

$$E_s = E_{0,s} e^{i(\omega t - ks)} \tag{1.3.2}$$

A similar equation holds for the azimuthal magnetic field.

For a cylindrical cavity it is more adequate to use cylindrical coordinates. The azimuthal field component varies periodically with the azimuth θ and therefore $\partial^2/\partial\theta^2 = -n^2$, where n is the periodicity. With this eq. (1.3.1) yields for the longitudinal component E_s:

$$\frac{\partial^2 E_s}{\partial r^2} + \frac{1}{r}\frac{\partial E_s}{\partial r} + \left(k_c^2 - \frac{n^2}{r^2}\right) \tag{1.3.3}$$

where the cutoff wave number k_c is defined by:

$$k_c^2 = \frac{\omega^2}{c^2} - k^2 \tag{1.3.4}$$

This differential equation can be solved with Bessel functions. The solution depends on the periodicity n, the so called modes of the cavity. Transverse magnetic and electric field components can be derived from (1.3.4) using Maxwell's curls equations and exhibit a similar mode structure.

The modes can be classified into two main groups, the TE modes, with only transverse electric field components and the TM modes, with only transverse magnetic field components. For particle acceleration only the TM modes can be used as they posses a longitudinal electric field component. Each mode is characterized by three indices $\mathrm{TM_{npq}}$, where n is the azimuthal periodicity, p the radial periodicity and q the longitudinal. For acceleration e.g. the $\mathrm{TM_{010}}$ would be adequate as it has a longitudinal field component. In most cases the fundamental mode of the structure is used for acceleration.

In order to obtain a travelling wave and not a decaying one, the wave number k_c^2 must be positive and we assume according to eq. (1.3.2) $\omega/c > k_c$ and define the cutoff frequency $\omega_c = ck_c$.

Important for particle acceleration is the phase and group velocity of the wave. For a cylindrical cavity the phase velocity v_{ph} is bigger than the speed of light while the group velocity v_g is smaller:

$$v_{ph} = \frac{c}{\sqrt{1 - \omega_c^2/\omega^2}} > c \qquad v_g = \frac{c^2}{v_{ph}} < c \tag{1.3.5}$$

1.3.2 Disk Loaded Waveguide

By introducing the right boundary conditions, the plane electromagnetic waves are modified to a wave with a non vanishing longitudinal electric field component, but with a phase velocity bigger than the speed of light. For particle acceleration the phase velocity must be equal to the particle velocity. This can be achieved by inserting metallic structures into the waveguide. The most common shape of these structures are disks, which are placed perpendicular to the waveguide axis, and the resulting waveguide is a *disk loaded waveguide* (fig. 1.3.1). The inserted disks create a sequence of cavities coupled through the central hole - the *iris*, which in total act as a band pass filter allowing electromagnetic fields of certain frequencies to propagate. By choosing the right geometry the desired frequency and phase velocity can be adjusted.

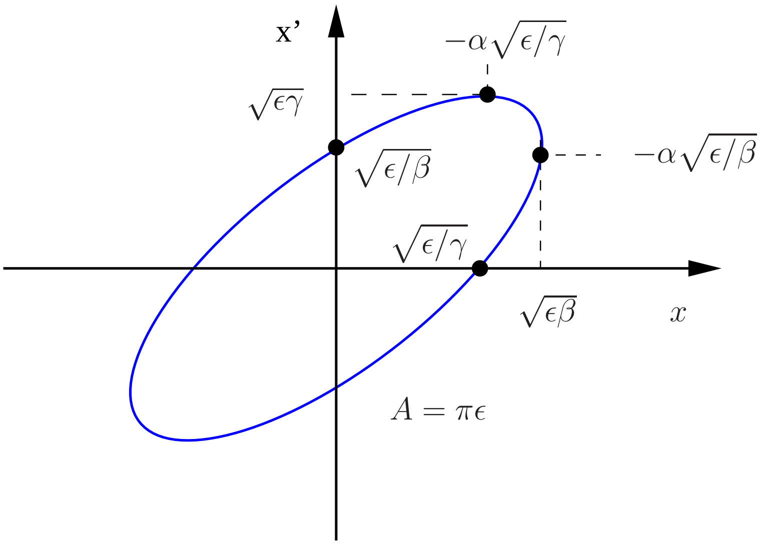

Figure 1.3.1: field in a cylindrical cavity and disk loaded waveguide

1.4 Synchrotron Radiation

The Maxwell equations and the theory of retarded potentials predict, that every moving charged particle looses energy in form of emitted radiation. This was first observed in 1974 at the 70 MeV synchrotron built at General Electric. Since then the radiation is called synchrotron radiation.

End of last century Lamor calculated the power of the radiation emitted by a nonrelativistic particle ($v \ll c$) with charge e moving with a momentum $\vec{p} = m_0\vec{v}$ [1]:

$$P_s = \frac{e^2}{6\pi\epsilon_0 m_0^2 c^3}\left(\frac{d\vec{p}}{dt}\right)^2 \tag{1.4.1}$$

The angular distribution of the radiation is identical with the one of a Hertzian dipole (fig. 1.4.1).

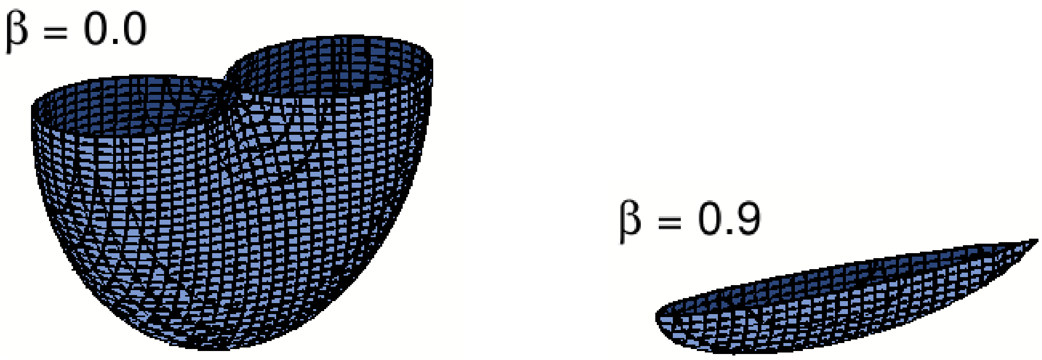

Figure 1.4.1: Angular distribution of Synchrotron radiation: In the rest frame of the electron ($\beta = 0.0$), the angular distribution is equivalent to the one of a Hertzian dipole and has a toroidal shape. In the laboratory system for an electron with ($\beta = 0.9$) it changes to a conical shape due to the Lorentz boost.

In accelerator physics, the particles normally have relativistic velocities ($v \approx c$) and (1.4.1) changes to:

$$P_s = \frac{e^2 c}{6\pi\epsilon_0 (m_0 c^2)^2}\left[\left(\frac{d\vec{p}}{d\tau}\right)^2 - \frac{1}{c^2}\left(\frac{dE}{d\tau}\right)^2\right] \tag{1.4.2}$$

where τ is the time in the restframe of the electron (fig. 1.4.1).
The radiation power depends on the direction of motion and acceleration of the particle. In the following the case of linear ($\frac{d\vec{v}}{d\tau} || \vec{v}$) and circular acceleration ($\frac{d\vec{v}}{d\tau} \perp \vec{v}$) will be treated in more detail .

1.4.1 Linear Acceleration

For linear acceleration (1.4.2) yields [1]:

$$P_s = \frac{e^2 c}{6\pi\epsilon_0 (m_0 c^2)^2}\left(\frac{dp}{dt}\right)^2 \tag{1.4.3}$$

So in a linear accelerator the energy loss caused by synchrotron radiation is very small. This can be shown with a simple example. If the energy gain per meter is dE/dx and we assume that the particles are relativistic, then the efficiency - the ratio between the radiated power and the power gained by the acceleration - yields:

$$\frac{P_s}{dE/dt} = \frac{P_s}{v dE/dx} = \frac{e^2}{6\pi\epsilon_0 (m_0 c^2)^2}\frac{1}{\beta}\frac{dE}{dx} \tag{1.4.4}$$

E.g. for an acceleration per meter of $dE/dx = 15\ \mathrm{MeV/m}$, the efficiency is 5.5×10^{-14} and in comparison for TBONE with a higher acceleration per meter $dE/dx = 30\ \mathrm{GeV/m}$ the efficiency is 1.1×10^{-6}, which is in both cases very small.

1.4.2 Circular Acceleration

If a particle is following a circular orbit, the emitted radiation is [1]:

$$P_s = \frac{e^2 c \gamma^2}{6\pi\epsilon_0 (m_0 c^2)^2} \left(\frac{dp}{dt}\right)^2 \overset{dp/dt = p \cdot v/R}{=} \frac{e^2 c}{6\pi\epsilon_0 (m_0 c^2)^4} \frac{E^4}{R^2} \tag{1.4.5}$$

where R is the bending radius of the particle orbit. Accordingly the synchrotron radiation power:

- is larger for particles with a smaller rest mass ($\sim \frac{1}{m_0^4}$).
- increases with the energy of the particle, so becomes more relevant for high beam energies ($P_s \sim E^4$).
- increases with decreasing bending radius ($\sim \frac{1}{R^2}$).

1.4.3 Coherent Synchrotron Radiation (CSR)

A particle bunch always emits coherent as well as incoherent synchrotron radiation. Coherent radiation is only emitted with wavelengths equal or larger than the bunchlength (fig. 1.4.2). Commonly the wavelength are very large and are cut off by the beampipe. Therefore the bunchlength has to be very short in order to make the coherent part of the radiation accessible.

The advantage of coherent synchrotron radiation is that the radiation power increases quadratically with the number of particles per bunch instead of linearly in the case of incoherent radiation.

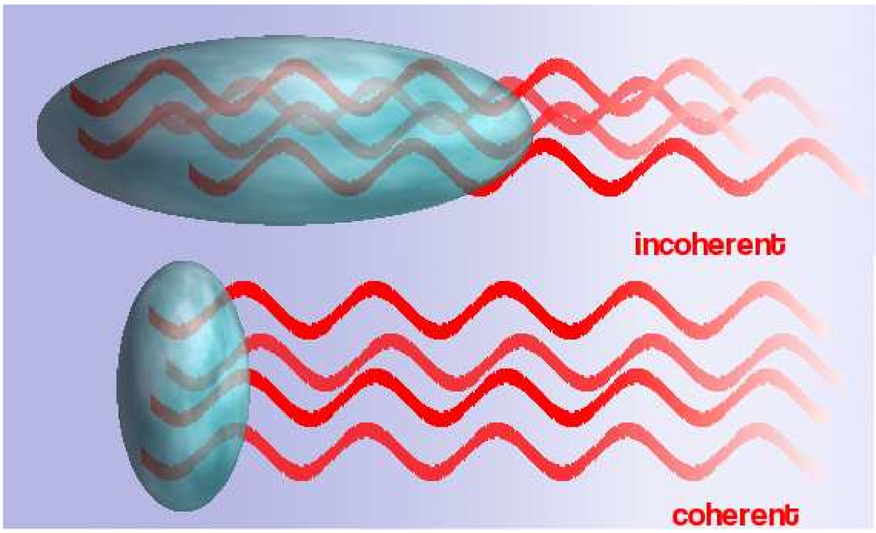

Figure 1.4.2: Coherent and incoherent synchrotron radiation: the radiation is coherent, if the wavelength is equal or larger than the bunch length.

Chapter 2

CLIC

The large hadron collider (LHC) will be the first accelerator in the multi TeV range. Many open questions will be hopefully answered by the experiments at the LHC, but there is a good chance that some of the problems will be left unsolved. Some of them may best be addressed by a lepton-antilepton collider.

As the energy loss per turn due to synchrotron radiation scales with $1/m^4$ and is thus much larger for electrons than for protons, it is not feasible to built a circular electron-positron collider. Therefore, present studies of future lepton-antilepton colliders in the TeV range focus on linear electron-positron accelerators. The Compact LInear Collider (CLIC) is a possible design for a linear electron-positron collider in the TeV range based on the two beam acceleration technique. It has been shown that with this technique center-of-mass energies from $500\ \mathrm{GeV}$ up to $5\ \mathrm{TeV}$ and a luminosity in the range of $10^{34}\ \mathrm{cm}^{-2}\mathrm{s}^{-1}$ could be reached. The physics experiments require a luminosity of at least $10^{34}\ \mathrm{cm}^{-2}\mathrm{s}^{-1}$ and a minimal center-of-mass energy of $1\ \mathrm{TeV}$. The CLIC design study presently concentrates on a center-of-mass energy of $3\ \mathrm{TeV}$ and a luminosity of $5.9 \times 10^{34}\ \mathrm{cm}^{-2}\mathrm{s}^{-1}$. A description of CLIC as well as the latest parameters can be found in [4] and [5].

2.1 CLIC RF Power Production and the Two Beam Acceleration Technique

To reach the design energy of $3\ \mathrm{TeV}$ within a reasonable accelerator length $< 40\mathrm{km}$ the accelerating gradient has to be very high ($100\ \mathrm{MV/m}$). Because superconducting technology as used for the International Linear Collider (ILC) is limited to lower gradients ($< 50\mathrm{MV/m}$) [6], room temperature travelling wave structures have to be used. The most obvious idea would be to generate the rf pulses with klystrons. Following this idea, the together 42 km long main linacs would have to be equipped with X-Band klystrons producing short pulses. This would be of course very costly. Instead a more cost efficient

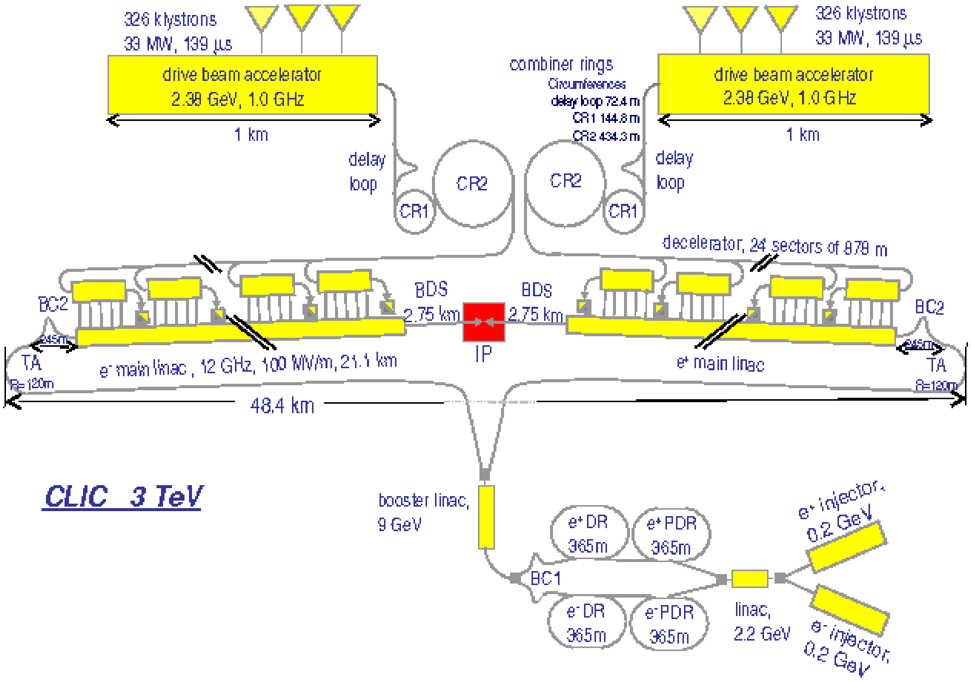

Figure 2.0.1: Schematic layout of CLIC for a design energy of 3 TeV and a frequency of 12 GHz: the bottom half shows the main beam complex, the upper part the drive beam complex, which will act as the power source for the main linac.

and promising way of producing high accelerating gradients at high frequencies is the two beam acceleration technique [7].

The principle of the two beam acceleration technique is to transform long rf pulses with low frequency, which are easy to produce by standard klystrons, into short rf pulses with high frequency and peak power. The manipulation of the rf pulses is done with the help of a high intensity electron beam, the so called drive beam. The advantage of electron beam manipulation compared to manipulation of rf pulses is that beam pulses can be transported over long distances with very low losses and be highly compressed.

Using a single drive beam pulse continuously decelerated along the linac length, would require very short pulses of high energy and current. Such pulses would be very challenging to create, accelerate and manipulate. Instead the parallel section is divided into 24 smaller units, the so called decelerators. In each decelerator one train is decelerated from the initial to a minimal energy supplying the power required to accelerate the main beam along the length of one decelerator.

2.2 Main Beam

The general layout of the main linac consists of the injector complex, the transfer line and the main accelerator (fig. 2.0.1). All parameters as well as more information can be found in [5].

2.2.1 Injector Complex

CLIC is designed for a polarized electron beam and an unpolarized positron beam. The injector complex consists of a positron and polarized electron source, an injector linac and pre-damping and damping rings (fig. 2.2.1)

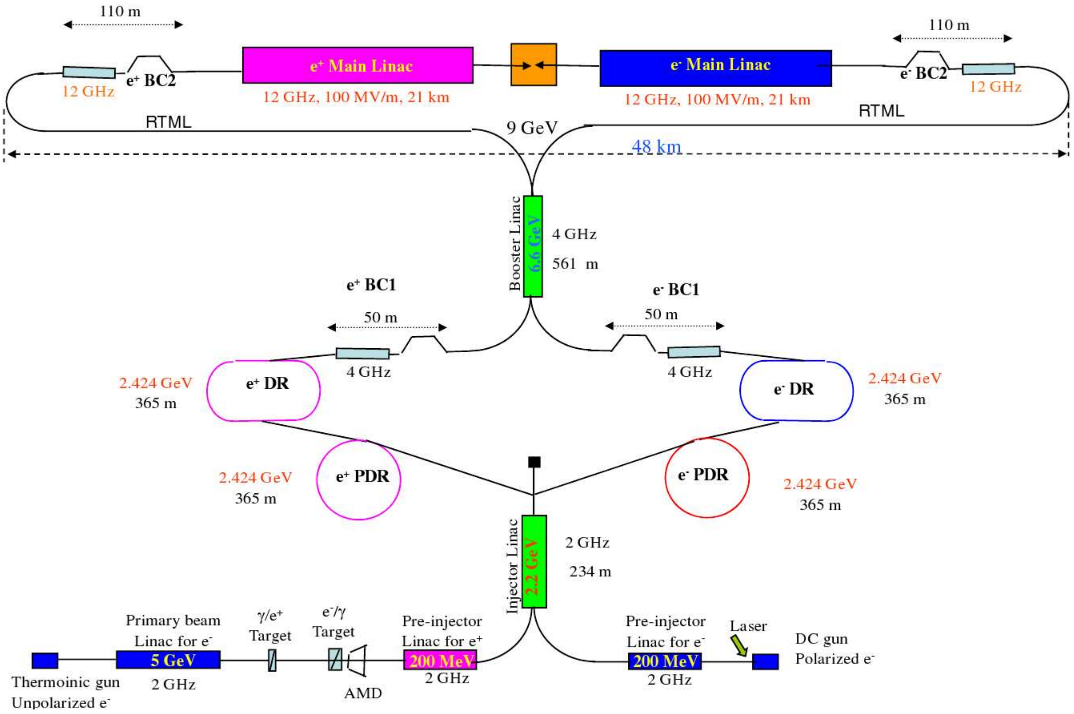

Figure 2.2.1: Main linac injector complex

Electron Source

The polarized electron beam is produced using a high-voltage DC photo injector. A laser which provides already the final time structure of the beam hits a GaAs cathode situated in a high voltage gun. The gun is designed to deliver 4.4×10^9 electrons with 80 % polarization to the entrance of the pre-damping rings. A 2 GHz L-band linac will accelerate subsequently the polarized electrons to 200 MeV followed by a 2.2 GeV linac at the same frequency. This injector linac also serves as positron accelerator (fig. 2.2.1). Because the positron beam has by far the largest transverse emittance, the constraints for the injector linac are set by the positron beam and not the electron beam. With the exception of the peak current the key parameters of this source have been achieved in existing or past polarized electron sources.

Positron Source

For the positron generation a $5\ \mathrm{GeV}$ electron beam is sent to a tungsten single crystal target. It produces photons and electron-positron pairs. Electrons, positrons and photons are separated by a dipole magnet. An Adiabatic Matching Device (AMD) with a magnetic field varying from $7\ \mathrm{T}$ to $0.5\ \mathrm{T}$ is used to prepare the positron beam for the injection into the first accelerating structure [8]. In a large acceptance L-band linac with a different design than the corresponding $200\ \mathrm{MeV}$ electron linac, the positrons will be accelerated first to $200\ \mathrm{MeV}$ and subsequently to $2.2\ \mathrm{GeV}$ by the injector linac shared with the electron beam.

Pre-damping Rings and Damping Rings

In order to reach the design luminosity, the emittance constraints for the main linac are very tight. For the emittance reduction pre-damping and damping rings are used. Due to the different generation of the positron and electron beam, the positron beam will have a considerably larger emittance than the electron beam and is therefore the more challenging beam in respect to beam size reduction.

To decouple the wide aperture requirements for the positron beam from the final emittance requirements of the main linac, the beam is pre-damped in a pre-damping ring with a large dynamic acceptance and relatively large equilibrium emittances. The pre-damping ring is followed by a damping ring with a racetrack like layout and a total length of $365.2\ \mathrm{m}$ (fig. 2.2.2). The two arcs contain theoretical minimum emittance (TME) cells and the straight sections FODO cells with damping wigglers or ending with dispersion suppressors or an injection/extraction region or rf cavities. A pair of sextupoles is responsible for the chromaticity corrections. The beam dynamics of the damping rings are dominated by intrabeam scattering due to the relatively small energy, small beamsize and high current.

The emittance of the electron beam after the injector would be small enough to do without a pre-damping ring. The reason for the additional pre-damping ring is the reduction of the damping time, so that the electron and positron beam keep synchronised [9].

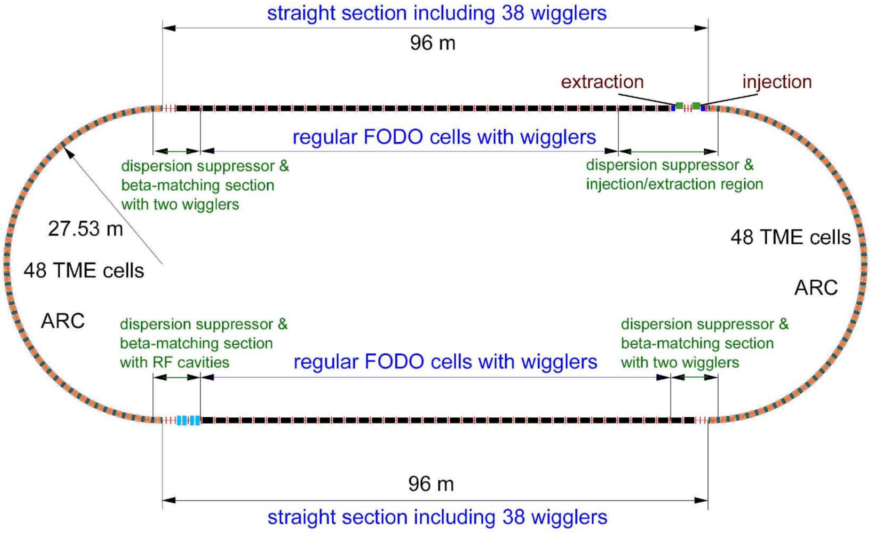

Figure 2.2.2: Schematic layout of the CLIC damping rings

2.2.2 Booster Linac, Right To Main Linac (RTML)

The transfer line from the damping rings to the main linacs includes the bunch compression, the acceleration to $9\ \mathrm{GeV}$ in the booster linac and the RTML (fig. 2.2.1). The main challenge is to preserve the beam quality obtained in the damping rings until the end of the transfer line.

The bunch compression is done in two stages: first in front of the Booster linac to shorten the bunch for acceleration and finally at the entrance to the Main linac. Each chicane consists of four magnets and compresses bunches first by a factor nine and finally by a factor four [10]. rf cavities are placed in front of each bunch compressor to introduce the right energy chirp for the compression. For the 270 degree turn around loop at the beginning of each linac special optics was designed to preserve the emittance taking coherent synchrotron radiation and intrabeam scattering effects into account.

2.2.3 Main Linac

The rf power for the main linac is supplied by the drive beam and transfered from the PETS (ch. 2.1) to the main accelerating structures. To facilitate the matching of the optics of the two beamlines the different structures are combined in modules, where each module consists of four PETS, each providing the power for two accelerating structures (fig. 2.2.3). The necessary focusing is performed with a conventional FODO lattice. The quadrupoles are part of the modules and replace up to four of the cavities. A beam position monitor is placed in front of each cavity [11].

The beam dynamics of the main beam are strongly influenced by the wakefield effects.

Transverse wakefields are mostly responsible for the emittance growth, which is compensated by the quadrupole focusing of the beam. Longitudinal wakefields induced from the head of the bunch are decelerating the tail and introduce an energy spread in each bunch. For this reason the beam is accelerated below transition.
For acceleration waveguide damped structures are used. To reduce the effect of long-range as well as short-range transverse wakefields on the beam, the accelerating structures were carefully designed and optimized. A description of the present structure design can be found in [5].

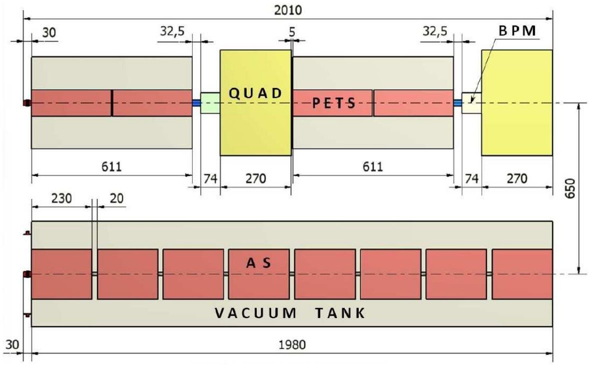

Figure 2.2.3: Schematic layout of one CLIC module. The drive beam is shown on top and the main beam on the bottom. One PETS supplies the power for two accelerating structures.

2.3 Drive Beam

The purpose of the drive beam is to provide the power for the main beam acceleration (ch. 2.1). The general layout of the drive beam complex is shown in fig. 2.0.1. It consists of the drive beam accelerator, the drive beam manipulation section, the transfer line and the parallel section consisting of 24 decelerators per linac. As the drive beam decelerator is not the main topic of this thesis, only a short summary of the main issues will be given in the following. A more detailed description with emphasis on the beam dynamics can be found in [12].

2.3.1 Drive Beam Generation

After gun and injector the drive beam is a $140\ \mu\mathrm{s}$ long electron beam. By accelerating it to approx. $2.4\ \mathrm{GeV}$ with a linear accelerator powered by klystrons, the energy of the long rf pulses is stored in the beam. The accelerating structures of the linac are fully loaded, so that about 98 % of the rf power are transfered to the beam (fig. 2.3.1). After the acceleration the beam pulse is composed of 24×24 sub-pulses, each $240\mathrm{ns}$ long.

In each sub-pulse the electron bunches occupy alternately only the even or odd buckets of the drive beam accelerator. The long pulse then passes through a delay line, where a rf deflector combines the bunches, so that the delayed bunches are placed between the bunches of the following sub-pulse. After the delay loop the whole pulse consists of 12×24 sub-pulses. The sub-pulses are then combined again by two consecutive combiner rings, first by a factor 3 to 4×24 and then by a factor 4 to obtain the final 24 sub pulses or trains required for the main linac (fig. 2.3.2). Each final train consists of 2928 bunches with a charge of $8.4\ \mathrm{nC/bunch}$ and an energy of 2.4 GeV. The trains are then transported via a common transfer line to the section, where main and drive beam run parallel to each other but in opposite directions. Pulsed magnets deflect each train at the appropriate time into a turn around loop leading to the correspondant decelerator, where the beam is decelerator in Power Extraction and Transfer Structures (PETS) (ch. 2.2) by 90 % of its inital energy and the output-power transfered to the main beam accelerating structures. At the end of one decelerator the beam is dumped and the next train is used to accelerate the main beam along the next unit.

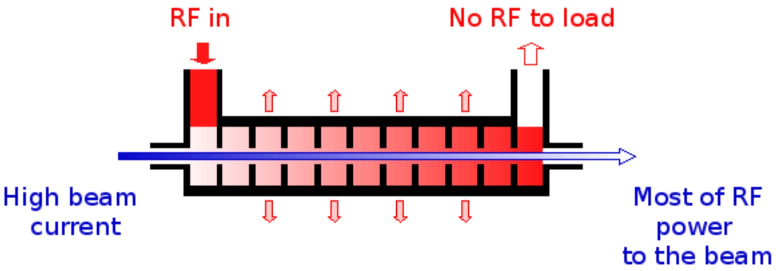

Figure 2.3.1: Fully loaded structure

2.3.2 Power Extraction and Transfer Structures (PETS)

The PETS is basically a travelling wave-structure with a fundamental mode frequency of $12\ \mathrm{GHz}$, where rf power is produced instead of being absorbed (fig. 2.3.3). The functional principle of the PETS is not fundamentally different from any travelling wave accelerating structure. Simplified, in order to extract power from the beam, the steps in the process of acceleration are taken in reversed order. A charge passing through the PETS excites the fundamental mode and the field of this mode will travel along the PETS trailing behind the charge with a velocity $v_g < c$. At the end of the PETS the field of the excited mode travels out of the structure and is transfered to the main accelerating structure of the main linac.

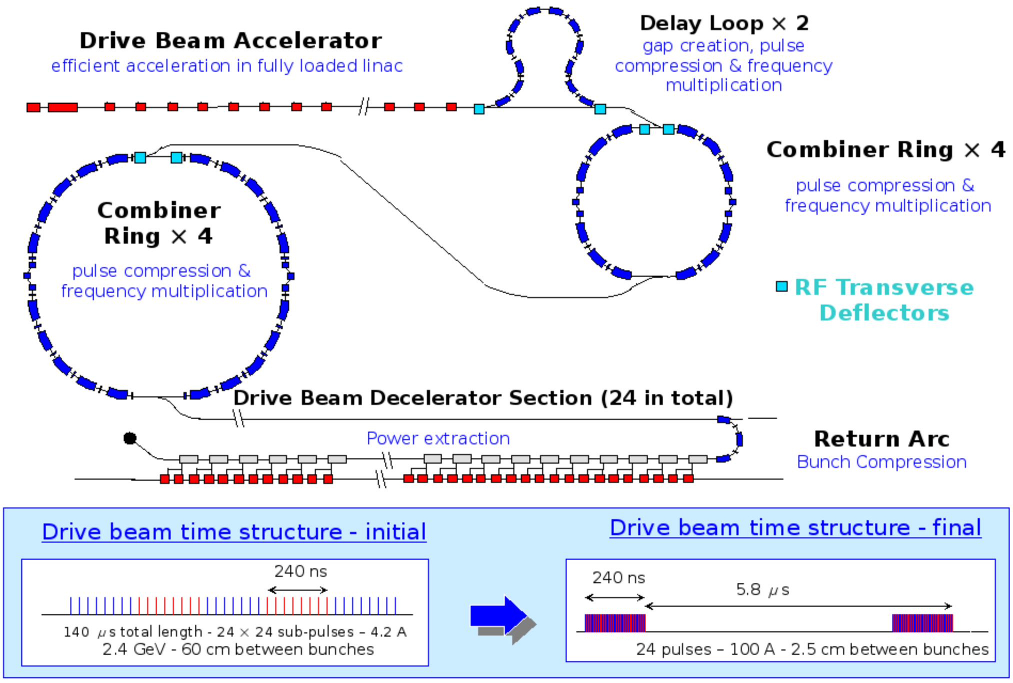

Figure 2.3.2: Schematic layout of one CLIC rf power source complex

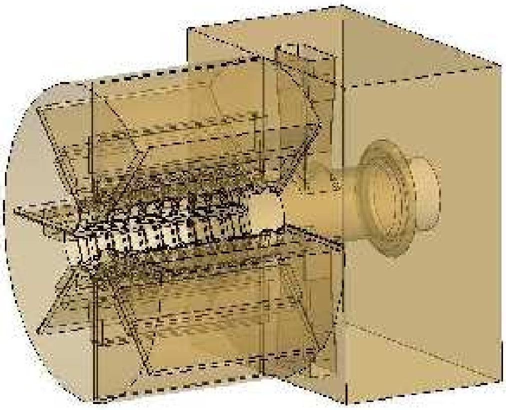

Figure 2.3.3: CLIC module

2.3.3 Decelerator Beam Dynamics

In this chapter we want to give only a short summary of the beam dynamics studies for the decelerator, which are documented in [12].

The decelerator beam dynamics are dominated by the effect of the PETS wakefields on the beam. The beam experiences two main effects in the PETS: the desired deceleration caused by the longitudinal wake field of the fundamental mode and the effect of higher order mode wakefields leading to unwanted behaviour of the beam. In [12] the dipole mode has been studied in detail, but the influence of wake fields from quadrupole or higher order moments have not been inspected in any work.

Deceleration

Beam particles, which pass the PETS excite the fundamental mode and the resulting wakefield decelerates trailing particles. At the end of each PETS the field is then coupled out and transfered to the main linac. A trailing charge therefore sees the sum of the wakefields of all particles ahead of it except the part, which has already left the PETS. This leads to a smaller deceleration of particles in the head and tail of one bunch and a larger deceleration of particles in the center (fig. 2.3.3). The second effect is, that the deceleration of the bunches increases along the beam until the "steady state" is reached, where each bunch sees the same decelerating field (fig. 2.3.3).
Following the baseline specification the most decelerated particle looses 90% of its energy along the whole decelerator. This stands in contrast to the least decelerated particle, which almost maintains its energy throughout the whole decelerator. This behaviour causes a large asymmetric energy spread in the beam and in one bunch, which is very unusual for common beams and is a characteristic of the drive beam.

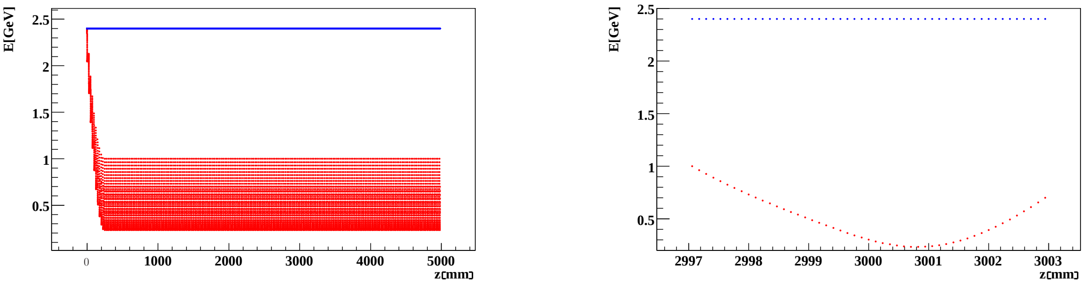

(a) Beam energy profile

(b) Bunch energy profile (steady state)

Figure 2.3.4: Beam energy profile at injection, in blue, and at the end of one decelerator, in red.

Lattice Design and Transverse Focusing

The PETS are designed to supply the power for two accelerating structures. If other elements e.g. quadrupoles for transverse focusing are installed instead of accelerating structures in the main linac, the corresponding PETS will have to be substituted by drift lengths. This leads to different lengths of the decelerators as in every decelerator the same energy must be extracted from the beam.
While the longitudinal wakefields are responsible for the deceleration, the transverse

wakefields cause a transverse deflection of the beam particles resulting in a large emittance growth. To compensate for this effect one FODO cell per module will be installed. Between each quadrupole none, one or two PETS will be placed depending on the number of accelerating structures (fig. 2.2.3). The quadrupole strength is adjusted, so that the most decelerated particle experiences a constant normalized quadrupole strength along the lattice. It is obvious that only a small fraction of the beam particles will be focused in an optimal way, which implies that a small energy spread is required at injection and a large emittance growth is expected along the decelerator despite the strong focusing.

Energy Acceptance of the decelerator

2.4 CTF3 - CLIC Test Facility 3

Chapter 3

TBONE - THz Beam Optics for New Experiments

Present experiments in condensed matter science inspecting e.g. superconductivity and behaviour of correlated electron systems as well as biological application like protein folding, solvation and biological interfaces demand an analysis with radiation in the THz to mid-IR range. THz and IR radiation can be for example generated by short pulse lasers, table top sources like thermal radiators and Free Electron Lasers, but none of the presently known sources delivers intense radiation in the whole spectral region. Therefore spectroscopic applications are restricted and a new intense radiation source would open the door for new science [13],[14].

The proposed lighthsource TBONE (THz Beam Optics for New Experiments) is a linac based coherent radiation source in the THz to mid-IR, which would fullfill all these requirements. To achieve a spectral range as broad as possible with a sufficient high time averaged power, the effective pulse length should be of the order of $5\ \mathrm{fs}$ and the repetition rate around $10\ \mathrm{MHz}$. For the purpose of spectroscopic studies an energy of $60\ \mathrm{MeV}$ would suffice, but in order to use TBONE also as a teststand for superconducting insertion devices the option for an energy of $100\ \mathrm{MeV}$ is kept. The design parameters of TBONE are given in table 3.0.1.

To achieve the presented design parameters one choice would be a superconducting electron linac. The proposed lattice layout is shown in fig. 3.0.1. As electron source two options are considered: a DC photo emission gun [15] or and SRF photo injector [16]. The injection system is followed by 3 superconducting 9-cell TESLA cavities, which are for example used for the Daresbury energy recovery linac ALICE [17].After the linac an insertion device test stand will be installed followed by the bunch compression system. The bunch compression is the most critical issue as the desired pulse length of $5\ \mathrm{fs}$ is very small. One option for the bunch compression in TBONE would be a 4-dipole magnetic chicane [18]. To limit the divergence of the beam after the extreme compression

Frequency range	$0.1 - 150$ THz
Peak power	up to several MW
Pulse length	down to 5 fs
Repetition rate	10 MHz
Linac energy	$60 - 100$ MeV
Bunch charge	$10 - 100$ THz

Table 3.0.1: TBONE design parameters

a so-called “missing bend arc” is proposed for the magnetic lattice responsible for the generation of coherent radiation [14].

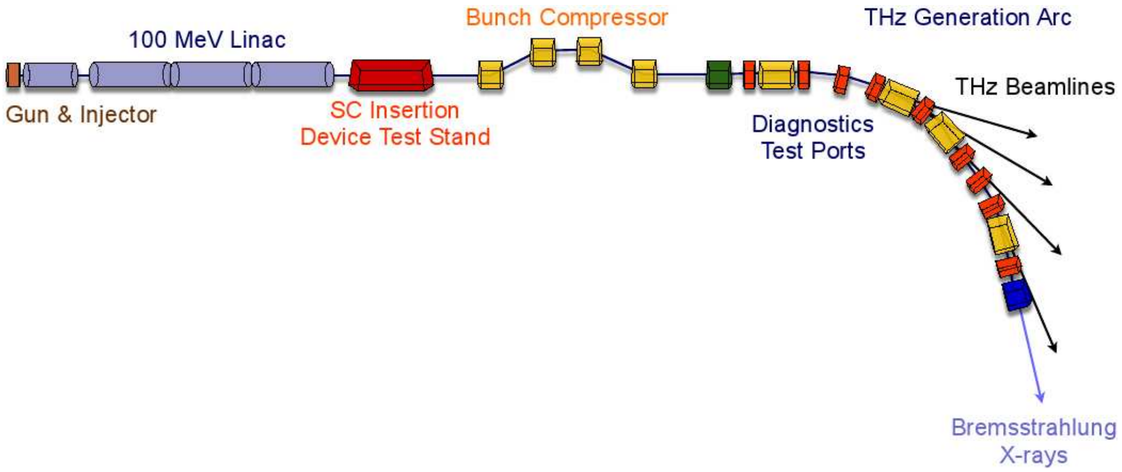

Figure 3.0.1: Lattice layout of TBONE. The lattice consists of injector and linac, insertion device test stand, bunch compressor and magnetic lattice for the generation of coherent radiation.

3.1 Injector System

For our simulations we chose the ALICE injector design as presented in [15]. The injector layout is shown in fig. 3.1.1.

The DC photocathode gun consists of a GaAs photocathode which will be illuminated by a laser beam from a $\mathrm{Nd:YVO_4}$ laser. At the end of the gun the emitted electrons will have an energy of $350\ \mathrm{keV}$. The gun is followed by a solenoid for focusing, a single-cell normal conducting buncher cavity operated at the fundamental linac frequency of $1.3\ \mathrm{GHz}$ and a second solenoid for further focusing. The Booster consists of two 9-cell superconducting cavities operated at $1.3\ \mathrm{GHz}$, where the electrons are accelrated to an energy of $8.35\ \mathrm{MeV}$. At the entrance of the first booster cavity the electrons have not

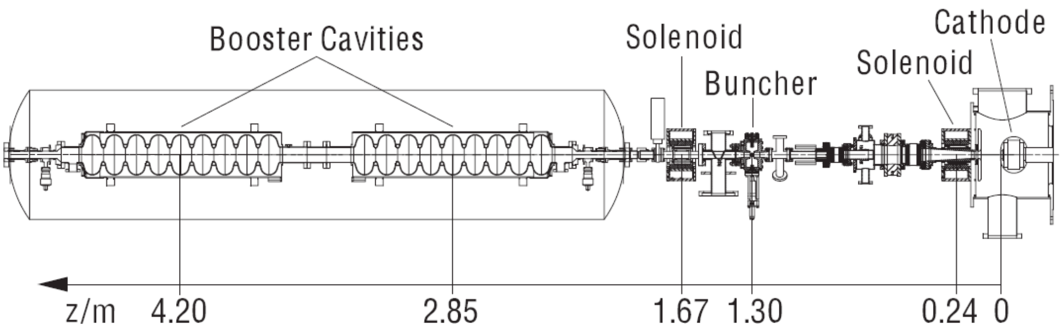

Figure 3.1.1: ALICE injector desing [15]

yet reached relativstic velocities and are therefore slightly decelerated in the first cell of the cavity. In the second cavity the beam is relativistic and the chosen cavity phase does not influence the bunchlength any more, but can induce an energy chirp in the beam. The beam parameters at the end of the ALICE injector taken from [15] are summarized in table 3.1.1. The beam distribution at the end of the ALICE injector does not meet

Parameter [unit]	**Symbol**	**Value**
norm. transverse emittance $[\mu\mathrm{m}]$	$\epsilon_{x,y}$	1.40
alpha function	$\alpha_{x,y}$	-2
beta function $[\mathrm{m}]$	$\beta_{x,y}$	15.0
bunch length $[\mathrm{mm}]$	σ_z	1.20
bunch length $[\mathrm{ps}]$	σ_z	4.0
Beam energy $[\mathrm{MeV}]$	E	8.35
Bunch charge $[\mathrm{pC}]$	Q_{bunch}	80.0
numb. of part. per bunch $[10^9]$	N_{bunch}	0.50

Table 3.1.1: Beam parameters after the injector for ALICE

all requirements for TBONE, but by a modification of the booster operation parameters could be pehaps adapted to our needs (shorter bunch length and rotated phase space beam ellipse). The injector system has not been studied yet and we therefore assume a beam distribution similar to the one after the ALICE injector, but adapted to TBONE. The modified parameters are summarized in table 3.1.2 and the beam distribution at the exit of the injector system shown in fig. 3.1.2.

In detail we have performed the following modification: We rotated the phase space ellipse, so that α would be equal to zero at the entrance of the linac, because a non-zero α would lead to a decrease or increase of the beam size, if no further focusing is done (this

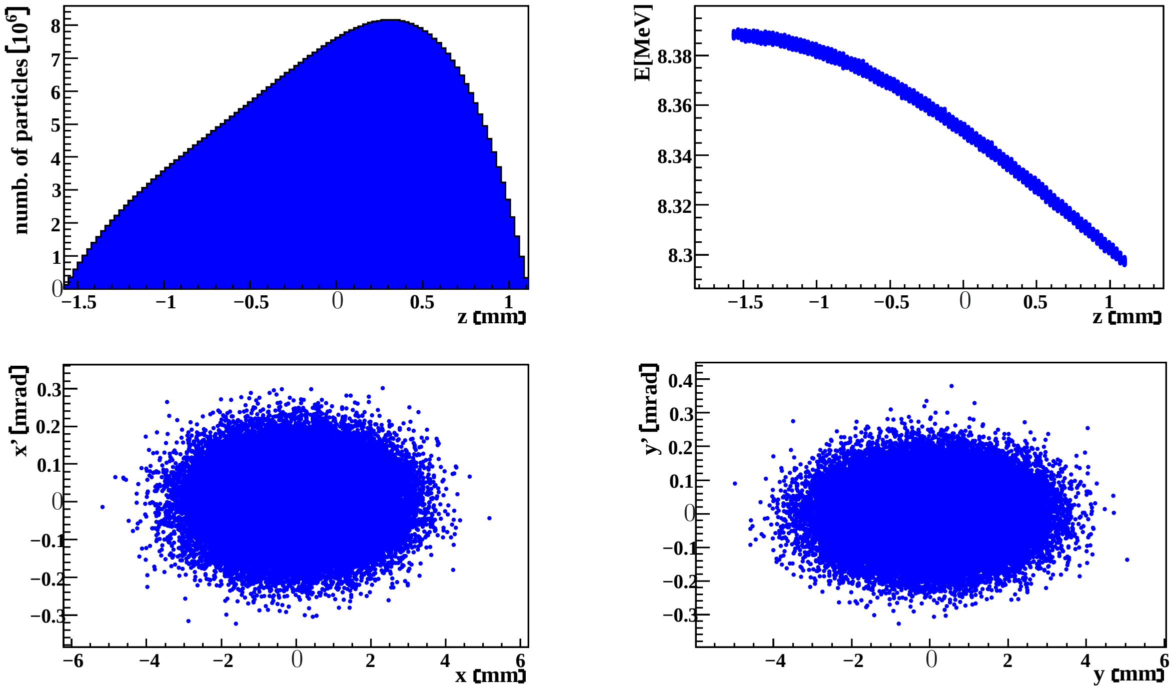

Figure 3.1.2: Beam distribution after the injector system for TBONE

is the case for TBONE). Such a rotation can be easily obtained by a change of the phase of the cavity. The bunch length at the exit of the ALICE injector system is by a factor 2 too large to reach the design bunch length of $5\ \mathrm{fs}$ after the bunch compressor. We therefore shortened the bunch by a factor 2. By a different operation mode of the first booster cavity and a better adaption of the laser, a shorter bunch length at the exit of the booster could perhaps be obtained. Another option would be to use the second proposed injector used at ELBE [16], which delivers the required bunch length but has an upper limit to the bunch charge of $77\ \mathrm{pC}$.

3.2 Superconducting Linac

The superconducting linac consists of three superconducting 9-cell TESLA cavities operated at a fundamental frequency of $1.3\ \mathrm{GHz}$ (fig. 3.2.1). As bunch distribution at the entrance of the linac we chose the modified distribution after the ALICE INJECTOR presented in ch. 3.1. For the generation of the longitudinal bunch and energy distribution we performed a polynomial fit to the charge and kinetic energy spread distribution at the end of the ALICE injector and shortened it by a factor 2.1 to obtain the required bunch length. A simulation of all beam particles is not possible out of simulation time reasons. Therefore we sliced the beam into 101 slices and reduced the number of particles to 101000.

Parameter unit	Symbol	Value
norm. transverse emittance $[\mu\mathrm{m}]$	ϵ_x	1.40
norm. transverse emittance $[\mu\mathrm{m}]$	ϵ_y	1.40
alpha function	$\alpha_{x,y}$	0
beta function $[\mathrm{m}]$	β_x	15.19
beta function $[\mathrm{m}]$	β_y	15.30
bunch length $[\mathrm{mm}]$	σ_z	0.62
bunch length $[\mathrm{ps}]$	σ_z	2.06
Beam energy $[\mathrm{MeV}]$	E	8.35
Bunch charge $[\mathrm{pC}]$	Q_{bunch}	83.86
numb. of part. per bunch $[10^9]$	N_{bunch}	0.52

Table 3.1.2: Modified beam parameters after the injector for TBONE

We defined the transverse distribution of each slices over the twiss parameters given in table 3.1.2. For the generation of the bunch distribution we used OCTAVE [19].

The beam dynamics simulation of the superconducting linac were performed with PLACET [20], which includes the simulation of the rf and wakefield kick in the cavities. The exact simulation method is described in [21]. The wakefield calculation is not straight forward and depend mainly on the structure, the beam structure and charge and bunchlength. An exact calculation of the wakefields would be out of scope of ours studies, but could be done at a later state with e.g. with GdfidL [22]. As a first approximate we used the wakefield calculation for the ILC main linac but with the bunch length and charge of TBONE as input parameters.

Figure 3.2.1: Superconducting 9-cell TESLA cavity

For the bunch compression a very large energy chirp in the beam is needed. By operating all three cavities above transition with rising phase of the cavity, some particles are decelerated and a large energy spread can be induced. For the first cavity we chose a phase of

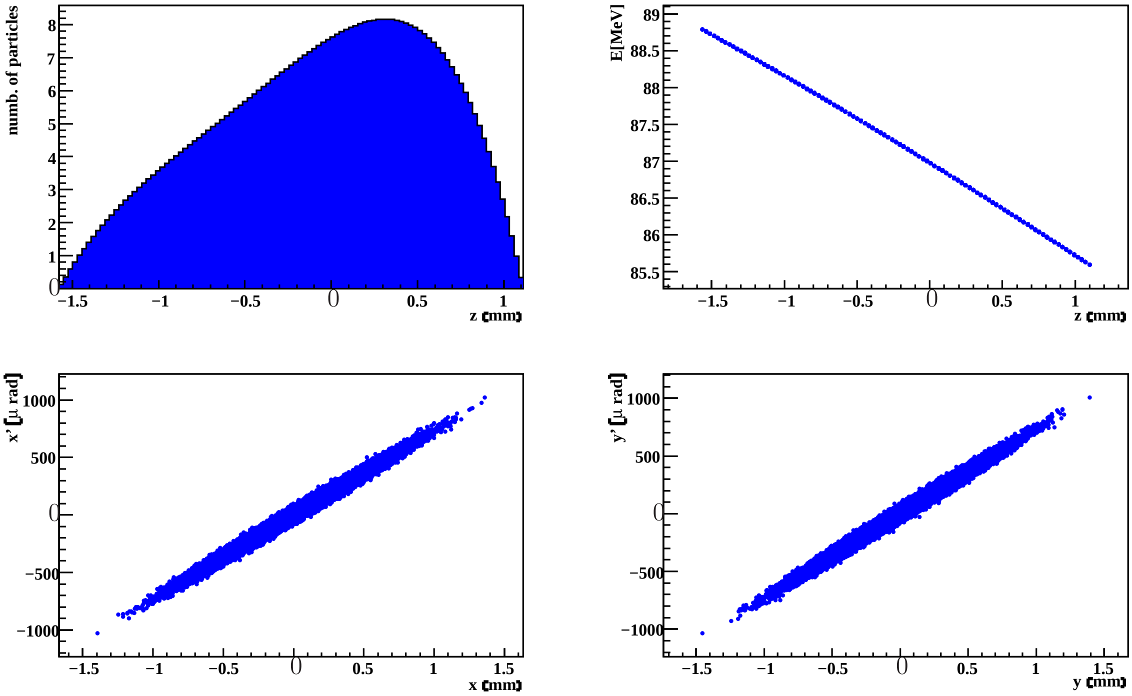

Figure 3.2.2: Beam distribution after the superconducting linac

$5.3\ ^\circ$, for the secon $40.3\ ^\circ$ and for the third $40.3\ ^\circ$. The distribution at the end of the linac is shown in fig. 3.2.2 and the final beam parameters in table 3.2.1

Parameter unit	Symbol	Value
norm. transverse emittance $[\mu\mathrm{m}]$	ϵ_x	1.40
norm. transverse emittance $[\mu\mathrm{m}]$	ϵ_y	1.40
alpha function	α_x	-8.44
alpha function	α_y	-8.50
beta function $[\mathrm{m}]$	β_x	11.56
beta function $[\mathrm{m}]$	β_y	11.64
bunch length $[\mathrm{mm}]$	σ_z	0.62
bunch length $[\mathrm{ps}]$	σ_z	2.06
Beam energy $[\mathrm{MeV}]$	E	87.02
Bunch charge $[\mathrm{pC}]$	Q_{bunch}	83.86
numb. of part. per bunch $[10^9]$	N_{bunch}	0.52

Table 3.2.1: Modified beam parameters after the injector for TBONE

3.3 Bunch Compression

The bunch compression is described in [18], where it is shown that a bunch length of 5 fs can be achieved. For these studies a slightly different distribution was assumed, but by optimizing the injector system and the operation mode of the cavities we are confident that a similar distribution with the required parameters can be delivered. The final bunch distribution is shown in fig. 3.3.1

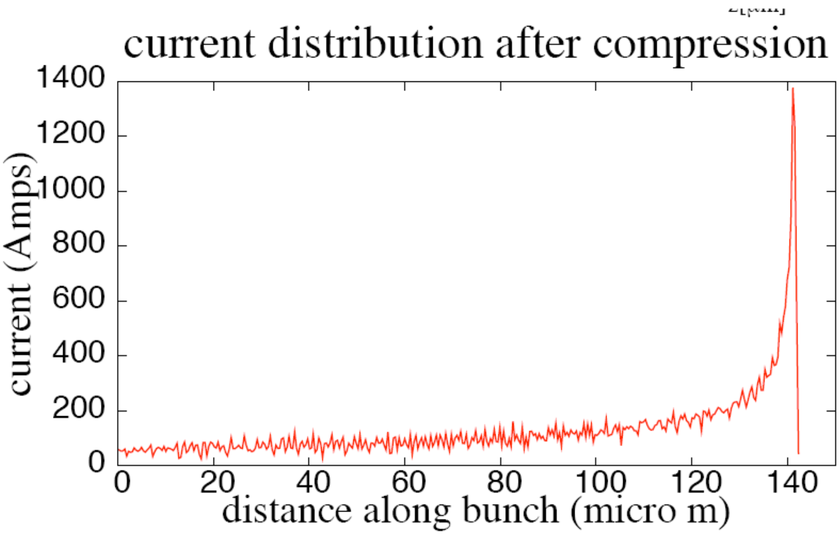

Figure 3.3.1: Longitudinal bunch distribution after the bunch compressor

Chapter 4

Halo and Tail Generation

If the amplitude of a beam particle increases significantly, it becomes a halo particle (fig. 4.0.1). Most experiments in particle physics require the collision of small and high energetic beams, so that luminosity and energy are sufficient for the investigation of improbable particle interactions. To detect even these infrequent events, it is necessary to minimize the background as much as possible. Halo particles can cause a growth of the beam size and though a loss in luminosity and can contribute significantly to background and radiation. Collimators near the interaction point stop most of the haloparticles, but by interacting with the material of the collimators, they can still produce an unwanted background of secondary muons.
Beside the unwanted generation of background and radiation, haloparticles can lead to beam losses in all parts of the accelerator.
Therefore halo and tail studies are needed even at an early stage of the development of future accelerators, to eliminate and estimate any performance limitations from this source.

Figure 4.0.1: Beam and Halo

4.1 Candidate Processes of Halo and Tail Generation

The increase of the amplitude of a beam particle and the associated generation of a halo particle can be caused by the following effects:
Particle processes:

- **Beam Gas Scattering and Multiple Scattering:**
  Beam particles perform elastic scattering (mott scattering) or inelastic scattering (bremsstrahlung) with the residual gas molecules. Multiple scattering can occur i.e. when beam particles hit a spoiler or any other dense material.

- **Spoiler Scattering:**
  Spoilers made of some dense material are often installed in front of Collimators to protect latter from e.g. overheating. Beam or Halo particles hitting the spoilers are stopped or perform multiple scattering.

- **Scattering of Thermal Photons (Inverse Compton Scattering):**
  Inverse compton scattering is the inelastic scattering process between an electron and a photon.

- **Synchrotron Radiation:**
  Synchrotron radiation photons are emitted by relativistic charged particles travelling in a magnetic field.

- **Residual Gas Ionization, Electron and Ion Cloud Effects:**
  Electrons or Ions can be accumulated near the beam and start interacting with the beam. This can cause serious instabilities.

- **Touschek Effect and Intrabeam Scattering:**
  The Touschek effect is a single scattering effect, where the small transverse momentum of two beam particles is transferred into a large longitudinal momentum. Both particles get lost, one with too much and one with too little energy. Intrabeam scattering is a multiple scattering effect with small scattering angles between beam particles. It leads to diffusion in all three dimensions and causes mainly a blow up of the whole beam instead of the direct loss of single particles.

- **Space Charge Effect:**
  The space charge effect is the effect of the electromagnetic self field of the beam on itself.

- **Beamloading and Wakefields:**
  The electromagnetic field of the bunch induces surface charges and currents in the

conducting walls of the surrounding structure. These fields can then act back on the beam particles.

Optics related effects:

- **Mismatch:**
  If the beam density contours do not coincide with the ellipse corresponding to the particle trajectories, the beam is mismatched. In this case the amplitude of some beam particles can increase significantly.

- **Coupling:**
  The movement of the particles in the horizontal and the vertical plane can be coupled. This is for example the case in sextupoles.

- **Dispersion:**
  The deflection of off momentum particles in any electric or magnetic field differs from the one of the reference particle. Dispersion is the beam dynamics effect of the momentum offset.

- **Nonlinearities:**
  Nonlinearities occur, when a lattice includes elements with non-linear electromagnetic fields, e.g sextupoles. Also field errors of quadrupoles or dipoles can be the source of nonlinearities.

- **Misalignment**
  If an element is misaligned, the beam particle experience a slightly other field depending on the extent of the misalignment. The error in the field experienced by the beam particles can cause an unwanted additional deflection of the beam particles.

Various other:

- **Noise and Vibrations:**
  Noise and vibrations of all different kinds can be transfered to the beam and lead to oscillations and emittance growth or even loss of the beam. For example rf noise can cause the generation of tails and lead to the loss of particles, which are situated close to the separatrix but still in the stable region. Or vibrations of elements e.g. quadrupoles can induce oscillations of the beam particles and emittance growth.

- **Dark Currents:**
  The walls of a structure can emit electrons. E.g. in an rf cavity these electrons are accelerated, which leads to in most cases negligible current conduction.

A more detailed description of most of the sources of halo and tail generation will be given in chapter 4.3 in the context of the low energy validation of PLACET-HTGEN.

4.2 Halo and Tail Simulation with PLACET-HTGEN

For the simulation of halo and tail generation we have used PLACET-HTGEN. The tracking code PLACET [23], [20] allows to simulate the beam dynamics of the main accelerating or decelerating part of CLIC and partly of the ILC. HTGEN [24] is a generic halo and tail generation package providing an interface to PLACET. An overview of the in the simulation included sources of halo and tail generation is given in table 4.2.1.
HTGEN was written for high beam energies. To be able to apply it also to middle and low energies, a critical review and low energy validation was carried out (ch. 4.3).
A description of the simulation technique and the used beam models is given in ch. 4.2.1 and ch. 4.2.2, while the particular motivation and challenges of the performed simulations are described in ch. 4.4 together with the obtained results.

Optics related effects:
Mismatch
Coupling
Dispersion
Nonlinearities
Misalignment

Various other
Noise and Vibrations
Dark Currents

Particle processes:
Beam Gas Scattering and Multiple Scattering
Spoiler Scattering
Compton Scattering
Synchrotron Radiation
Residual Gas Ionization, Electron and Ion Cloud Effects
Touschek Effect and Intrabeam Scattering
Space Charge Effect
Beam Loading and Wakefields

Table 4.2.1: 🟦 Included in PLACET 🟩 Included in HTGEN

4.2.1 Beam Models

Particle Beam Model

A particle beam consists of several bunches and each bunch of many particles, which are represented by a position in phase space $(x_i, x'_i, y_i, y'_i, E_i, z_i)$. To reduce the runtime the number of beam particles is normally scaled down. For halo simulation a particle beam model is more adequate as halo particles are generated by scattering of individual beam particles.

Sliced Beam Model

For high intensity beams it is better to use a sliced beam model, because the simulation of e.g. wakefield effects becomes easier and considerably faster. In the sliced beam model the beam consists of several bunches. Each bunch is cut into longitudinal slices and each slice consists of one or several macroparticles, which are represented by the position of the centroid in phase space $(x_i, x'_i, y_i, y'_i, E_i, z_i)$, the weight w_i and the sigma matrix σ_i defined by eq. (1.2.12). The weight of one macroparticle is proportional to the number of particles it represents. So the weights together with the position of the slices defines the longitudinal distribution of the beam (fig. 4.2.1). The exact definition of the weights can vary. In PLACET the sum over all weights must be one ($\sum_i w_i = 1$). The sigma matrix which belongs to each macroparticle gives information about the particle distribution, normally a gaussian distribution, it represents .

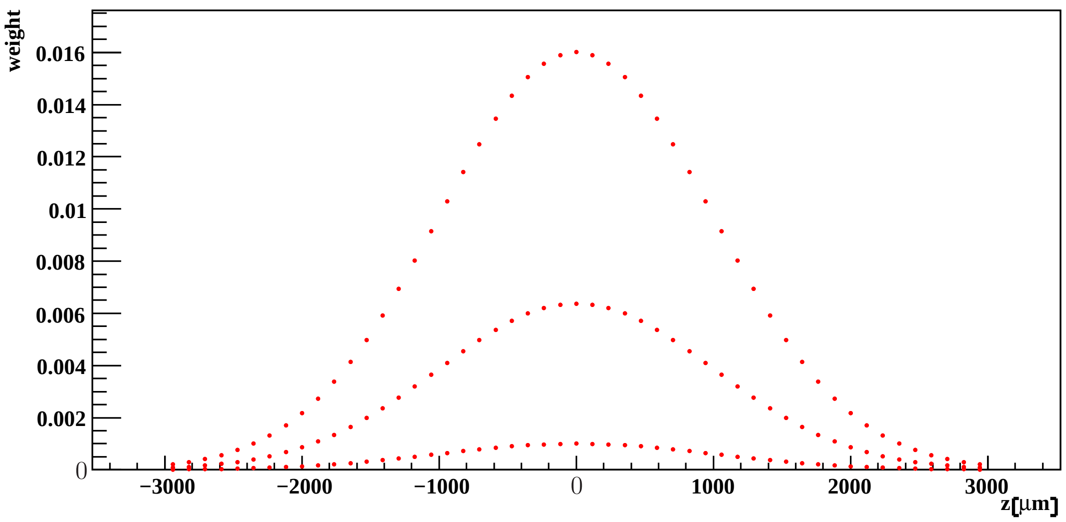

Figure 4.2.1: Example of a sliced beam: one bunch of the CLIC drive beam with 51 slices and 5 macroparticles per slice

4.2.2 Simulation Technique

Ch. 4.2.2 gives a general description of PLACET-HTGEN, while Ch. 4.2.2 describes in more detailed the implementation of the tracking in cavities and PETS.

General Description

HTGEN simulates the deflection of the beam particles due to beam gas scattering and multiple scattering. PLACET performs the tracking through the different elements including the simulation of several other halo sources (table 4.2.1). It is possible to define an initial halo, but for simplicity we assume, that there is no halo in the beginning of the beamline.

First the beam is tracked through the first element. Then HTGEN computes the number of scattered halo particles N_{scatt} given by:

$$N_{\text{scatt}} = P\ l\ N \tag{4.2.1}$$

where P is the scattering probability (B.0.2) of the specific process (mott scattering, bremsstrahlung or multiple scattering), l the length of the element and N the number of beam particles. After the calculation of the number of scattered particles, the individual particles are picked randomly out of the beam and scattered according to the scattering angle distribution of the process. In the case of a sliced beam the sigma matrix of the macroparticles is taken into account, when the halo particles are chosen out of the beam particles. After scattering, beam and halo are tracked through the next element. At the end of the element the in this element generated N_{scatt} halo particles are added to the existing halo and beam and halo are again tracked through the next element. This is repeated until the end of the beamline.

Halo Tracking in Cavities and PETS

In most elements it is sufficient to track the halo as a second beam through the beamline and neglect the influence of the beam on the halo. Instead in elements where collective effects like wakefields play a role the halo must be tracked together with the beam in order to obtain a realistic halo tracking. As the particle density of the halo is very small compared to the particle density of the beam, the halo does not effect the beam but the beam can effect considerably the halo.For the three accelerators studied, the affected elements are cavities and PETS, where the effect of wakefields can not be neglected.
A realistic tracking in general requires, that the halo particles are tracked in the same way as the beam particle, if the initial coordinates in the 6d-phase space coincide. On the other hand the halo particles shall not influence the beam.
For the tracking in cavities and PETS a sliced beam model of the beam is more adequate in order to provide an acceptable running time. Using this model all macroparticles of one slice experience the same wakefield and rf kick. For the halo particles a pure particle model was originally used. To be able to apply the same wakefield and rf kick to the halo and beam particles with a z-position in the same slice, a slicing of the halo beam was required. Therefor we have binned or sliced the halo beam but have not adapted the model of macroparticles as it is not suited for the simulation of the halo. Using this beam model for the halo, we have implemented the halo tracking in cavities and PETS, so that the halo and beam particles in the same slice experience the same rf and wakefield kick. A description of the simulation technique for the tracking of the beam and implicitly for the halo in cavities and PETS can be found in the manual [21].

Misalignment

The misalignment tolerances for CLIC are very tight (they lie in the $\mu\mathrm{m}$ range). Therefore the simulation of misalignment effects on the beam is rather essential and has been included in PLACET.
In the simulation the beam is translated or rotated depending on the type of misalignment at the beginning and end of each misaligned element, which is out of the principle of relativity equal to giving the elements themselves an offset. We have extended the simulation of misalignment by rotating or translating also the halo beam, so that the halo particles experience the same translation or rotation as the beam particles elements.

4.2.3 Benchmarking

A correct halo tracking requires, that halo and beam particles with the same initial coordinates in the 6d phase space follow exactly the same path and that the halo particles do not influence the beam particles. To benchmark the halo tracking a new routine has been written, which works in the following way:
An arbitrary beam is first defined, then all beam particles are copied and defined as new halo particles or rather test beam particles. After the definition of the test beam and beam, both are tracked through the beamline, which consists of elements to be tested.
If the coordinates of the beam particles match exactly with the coordinates of the corresponding test beam particles at the end of the beamline, the halo particles are tracked the same way as the beam particles, which proves the correct implementation of the halo tracking.
All elements used in the performed simulations (cavities, PETS, quadrupoles and drift lengths) have been benchmarked in this way and show a correct halo tracking.

4.3 Low Energy Validation of PLACET-HTGEN

TBONE, the CTF3 TBL and the CLIC drive beam are middle or rather low energy beams. Because HTGEN was written for high beam energies, a low energy validation of the simulation package had to be performed.

4.3.1 Beam Gas Scattering

Beam particles can perform elastic (mott scattering) or inelastic (bremsstrahlung) scattering with the molecules of the residual gas (fig. 4.3.1 and 4.3.2).

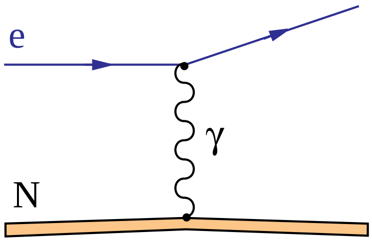

Figure 4.3.1: Mott Scattering

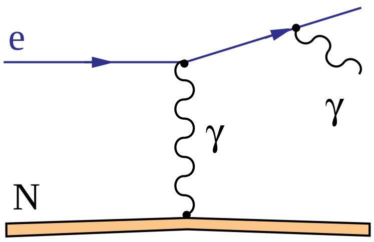

Figure 4.3.2: Bremsstrahlung

The molecule density n_{gas}, pressure p and temperature T are connected by the ideal gas equation:

$$p = n_{\text{gas}}\, k_B\, T \tag{4.3.1}$$

where k_B is the Boltzmann constant.

Elastic Beam Gas Scattering - Mott Scattering

The mott scattering differential cross section is given by [25]:

$$\left(\frac{d\sigma}{d\Omega}\right)_{\text{mott}} = \left(\frac{Zr_e}{2\gamma\beta^2 \sin^2\frac{\theta}{2}}\right)^2 \left(1 - \beta^2 \sin^2\frac{\theta}{2}\right) \tag{4.3.2}$$

The first term is the Rutherford cross section, which is multiplied by a second term in order to respect helicity conservation. The total mott cross section would be divergent for $\theta = 0$. In order to avoid this divergence a minimal deflection angle θ_{min} is introduced:

$$\sigma_{\text{mott}}\left(\theta_{\text{min}}\right) = \pi\left(\frac{Zr_e}{\gamma\beta^2}\right)^2 \left(\frac{1+\cos\theta_{\text{min}}}{1-\cos\theta_{\text{min}}} + \beta^2 \ln\left(\frac{1-\cos\theta_{\text{min}}}{2}\right)\right) \tag{4.3.3}$$

In the limit of highly relativistic electrons and small scattering angles ($\beta \approx 1$, $\theta_{\text{min}} < 0.05$), the terms except $(1+\cos\theta_{\text{min}})/(1-\cos\theta_{\text{min}})$ can be neglected.

$$\sigma_{\text{mott}}\left(\theta_{\text{min}}\right) = \pi\left(\frac{Zr_e}{\gamma}\right)^2 \left(\frac{1+\cos\theta_{\text{min}}}{1-\cos\theta_{\text{min}}}\right) \overset{\cos\theta_{\text{min}}\approx 1}{\approx} 2\pi\left(\frac{Zr_e}{\gamma}\right)^2 \left(\frac{1}{1-\cos\theta_{\text{min}}}\right) \tag{4.3.4}$$

For very small angles $\theta_{\text{min}} < 10^{-6}$ the term $1/(1-\cos\theta_{\text{min}})$ can lead to numerical instabilities and it is better to use the Taylor expansion of $(1-\cos\theta_{\text{min}}) \approx \theta^2/2$:

$$\sigma_{\text{mott}}\left(\theta_{\text{min}}\right) \approx \frac{4\pi Z^2 r_e^2}{\gamma^2 \theta_{\text{min}}^2} \tag{4.3.5}$$

Relevant for halo production are scattering angles which exceed the beam divergence, or roughly:

$$\theta_{\text{min}} = \sqrt{\epsilon/(\gamma\beta_y)} \tag{4.3.6}$$

where ϵ is the normalized emittance and β_y the local vertical beta function.

Eq. (4.3.4) and (4.3.5) are implemented in HTGEN.

Validity of HTGEN

The mott scattering cross section scales with $1/\gamma^2$ and therefore becomes more relevant for small energies (4.3.4). The approximation of $\beta \approx 1$ and $\theta_{\text{min}} < 0.05$ is still a good approximation for electron beams in the $10\,\text{MeV}$ range, so also for TBONE and the CLIC and CTF3 TBL drive beam. The minimal scattering angles given by (4.3.6) lie in the μrad to mrad and well below 0.05.

Inelastic Beam Gas Scattering - Bremsstrahlung

In the bremsstrahlung process the electron interacts with the field of one individual residual gas molecule and radiates a photon (fig. 4.3.2).
The first quantummechanical calculations of the bremsstrahlung/pair production cross section were published by H. Bethe and W. Heitler in 1934 [26]. Bethe and Heitler used the Born approximation and assumed, that the nucleus is infinitely heavy, pointlike and spinless, and its coulomb field screened by the atomic electrons. In general the Born approximation becomes worse as the atomic number of the target increases, the initial electron energy decreases and the photon energy approaches the high frequency region. The theory also doesn't model the screening effects properly, which become more relevant for very low electron energies and for targets with high atomic numbers. Between 1954 and 1959 the Bethe-Heitler theory was extended by Davies, Bethe, Maximom, Olsen and Wergeland (DBMOW theory) [27], [28], [29], [30]. They substituted the plane-wave functions used in the Born approximation by the better relativistic coulomb wave function, known as coulomb correction, and included screening in the formfactor calculation. These two corrections are nearly independent and additive at high energies [29]. The DBMOW theory is applicable in the high-energy region ($> 50\,\text{MeV}$), and tends to fail in the high frequency limit of the bremsstrahlung spectrum. In 1964 Drell and Walecka generalized the results of Bethe and Heitler to targets of arbitrary mass, spin and form factors and arbitrary final states [31] and made it possible to generalize the theory of bremsstrahlung. In 1974 Y. Tsai published a review of the DBMOW theory, where he used the Thomas-Fermi form factor model [32]. HTGEN is based on the Tsai formulas.

Cross Section after Tsai

At very high energies and except the high-energy tip of the bremsstrahlung spectrum, the bremsstrahlung cross section can be approximated in the complete screening case by [32]:

$$\frac{d\sigma}{dk} = 4\alpha r_e^2 \frac{1}{k}\left[\left(\frac{4}{3} - \frac{4}{3}y + y^2\right)\left(Z^2(L_{\text{rad}} - f) + Z L'_{\text{rad}}\right) + \frac{1}{9}(1-y)(Z^2+Z)\right] \tag{4.3.7}$$

where k is the photon energy, $y = k/E$ the photon energy in units of the beam energy, α the fine structure constant and r_e the classical electron radius. L_{rad} is derived from the

elastic form factor, L'_{rad} from the inelastic form factor and f is the coulomb correction.
In particle physics the bremsstrahlung cross section is often expressed in terms of the radiation length:

$$\frac{1}{X_0} = \frac{4\alpha r_e^2 N_A}{A}\left(Z^2(L_{\text{rad}} - f) + ZL'_{\text{rad}}\right) \tag{4.3.8}$$

and ignoring the term $(1-y)(Z^2+Z)$ in (4.3.7) the cross section becomes proportional to the radiation length. Subsequent multiplication by E yields:

$$\frac{d\sigma}{dy} = \frac{A}{N_A X_0}\frac{1}{y}\left(\frac{4}{3} - \frac{4}{3}y + y^2\right) \tag{4.3.9}$$

In the infrared limit the ignored term is approximately 2.5%.
The total cross section is obtained by integration of (4.3.9) over y from $y = y_{\text{min}}$ to $y = 1$:

$$\sigma_{\text{brem}} = \frac{A}{N_A X_0}\left(-\frac{4}{3}\ln y_{\text{min}} - \frac{5}{6} + \frac{4}{3}y_{\text{min}} - \frac{y_{\text{min}}^2}{2}\right) \tag{4.3.10}$$

A good value for y_{min} is 0.01.

Radiation length after Tsai
The radiation length X_0 of elements from $Z = 1$ to $Z = 92$ after Tsai is defined by:

$$\frac{1}{X_0} = \frac{4\alpha r_e^2 N_A}{A}\left(Z^2(L_{\text{rad}} - f) + ZL'_{\text{rad}}\right) \tag{4.3.11}$$

where r_e is the classical electron radius, N_A the Avogadro constant and α the fine structure constant. L_{rad} and L'_{rad} are given in table 4.3.1. For elements with $Z \geq 5$ Tsai uses the Thomas-Fermi-Molière approximation. The coulomb correction $f(Z)$ for elements up to $Z = 92$ can be represented to 4-place accuracy by

$$f(Z) = z^2\left((1+z^2)^{-1} + 0.20206 - 0.0369z^2 + 0.0083z^4 - 0.002z^6\right) \tag{4.3.12}$$

where $z = \alpha Z$.

Element	Z	L_{rad}	L'_{rad}
H	1	5.31	6.144
He	2	4.79	5.621
Li	3	4.74	5.805
Be	4	4.71	5.924
Others	≤ 4	$\ln(184.15Z^{-1/3})$	$\ln(1194Z^{-2/3})$

Table 4.3.1: Tsai's L_{rad} and L'_{rad}

A compact fit after Dahl of Tsai's formula provides an easy to implement formula and gives values better than 2.5% accuracy for all elements except Helium, where the result is 5% to low [33].

$$X_0 = \frac{A}{4\alpha r_e^2 N_A Z(Z+1)\ln(287/\sqrt{Z})} = \frac{716.408\ A}{Z(Z+1)\ln(287/\sqrt{Z})} \quad [\,\mathrm{g\ cm^{-2}}] \tag{4.3.13}$$

Often the residual gas consists of different gas molecules. In this case under neglection of the effect of molecular bindings the radiation length can be approximated by:

$$\frac{1}{X_0} = \sum f_i \frac{1}{X_i} \tag{4.3.14}$$

where f_i are the fractions by weight of elements i given by:

$$f_i = \frac{A_i}{\sum_{i=1}^{N} A_i} \tag{4.3.15}$$

where a_i is the number of atoms of the ith element of the molecule.

Accuracy of Tsai's theory

The formulas derived in the DBMOW and consequently also in Tsai's theory are estimated to have an accuracy of the order of $(Z/137)^2(\ln E/E)$ [34], so get less reliable for small energies, which corresponds approx. to an uncertainty of 3% for energies above $50\ \mathrm{MeV}$. This was also experimentally confirmed [35]. In the intermediate-energy region between $2\ \mathrm{MeV}$ and $50\ \mathrm{MeV}$ the high-energy approximations tend to fail and the formulas become more cumbersome, if at all assignable. Only very few measurements have been made in this energy region. There have been attempts of numerical calculation e.g. by Tseng and Pratt [36] and e.g. GEANT4 uses the Tsai formula down to $1\ \mathrm{GeV}$ and for lower energies a fit to the EEDL data set [37] with an estimated relative error of $\Delta\sigma/\sigma = 4 - 5\%$ for energies bigger than $1\ \mathrm{MeV}$ [38].

Landau Pomeranchuk Migdal (LPM) effect

The LPM effect is the suppression of photon production due to the multiple scattering of the electron. As the density of the atoms in the residual gas is very small multiple scattering becomes very improbable and with it also the LPM effect.

Molecular Bindings

The various theories apply only to a gas of free atoms. The effect of molecular bindings are very small, except for energies below $1\ \mathrm{keV}$ [39], but are significant in cristals, which is shown e.g. in [40].

Angular distribution

The angular distribution is of the form [41]:

$$f(\theta)d\theta = \frac{\theta}{(\theta^2 + \gamma^{-2})^2} \tag{4.3.16}$$

where θ is the angle between the initial electron and the emitted photon. The average angle is of the order $\theta \approx 1/\gamma$, which is e.g. for a beam energy of $100\ \mathrm{MeV}$ in the mrad range.

Validity of HTGEN

In HTGEN (4.3.13) and (4.3.10) are implemented. This is a good approximation for energies bigger than $50\ \mathrm{MeV}$, but tends to be less reliable for smaller energies. The assumption of complete screening might not be adequate for very low electron energies. The LPM effect can be neglected.
As the energy decreases mott scattering becomes more and more dominating and the exact calculation of bremsstrahlung less important. So HTGEN is in most cases also still valid for energies smaller than $50\ \mathrm{MeV}$.

4.3.2 Scattering of Thermal Photons - Inverse Compton Scattering

Inverse compton scattering is the inelastic scattering process of a photon with an electron resulting in an energy gain of the photon.

Thermal photons

Most of the photons originate from the black body radiation of the beampipe respectively the surrounding structure. The density and energy distribution is then given by the Plank formula [42]:

$$dn_p = \frac{\epsilon^2 d\epsilon}{\pi^2 c^3 \hbar^3 \left(e^{\epsilon/k_B T} - 1\right)} \tag{4.3.17}$$

where ϵ is the photon energy, c the speed of light, $\hbar$ the Boltzmann constant and T the absolute temperature of the black body in Kelvin.
The total number of photons per cm^3 is:

$$n_p = \frac{2.4(kT)^3}{\pi^2 c^3 \hbar^3} = 20.2\, T^3\ \mathrm{cm}^{-3} \tag{4.3.18}$$

and the average energy of the photons is:

$$\langle \epsilon \rangle = 2.7\, k_B T \tag{4.3.19}$$

Kinematics of Compton Scattering

The total compton cross section is [43],[42]:

$$\sigma_{\mathrm{compton}} = 2\pi r_e^2 \frac{1}{x} \left(\left(1 - \frac{4}{x} - \frac{8}{x^2}\right) \ln(1+x) + \frac{1}{2} + \frac{8}{x} - \frac{1}{2(1+x)^2} \right) \tag{4.3.20}$$

where r_e is the classical electron radius and x the dimensionless parameter:

$$x = \frac{4E\epsilon}{m^2c^4}\cos^2\frac{\alpha_0}{2} \tag{4.3.21}$$

E the initial electron, ϵ the initial photon energy in the laboratory system and α_0 the collision angle (fig. 4.3.3).

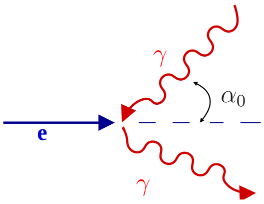

Figure 4.3.3: Kinematics of compton Scattering

In the nonrelativistic limit $x \ll 1$ the compton cross section can be approximated by:

$$\sigma_{\text{compton}} = \frac{8\pi r_e^2}{3}(1-x) \tag{4.3.22}$$

where the first term is the Thomson cross section $\sigma_{\text{T}} = 6.65 \times 10^{-25}$ cm$^-2$.
and in the ultrarelativistic limit $x \gg 1$ by:

$$\sigma_{\text{compton}} = 2\pi r_e^2\frac{1}{x}\left(\ln x + \frac{1}{2}\right) \tag{4.3.23}$$

The cross section and the mean free path length are normally small even for room temperature and therefore the deflection of the electrons by compton scattering negligible [44] . But the electron also looses energy in the scattering process, which can cause an energy spread leading to noticeable beam losses. The maximal energy spread caused by compton scattering is [42]:

$$\frac{\Delta E}{E} = \frac{\epsilon_{max}}{E} = \frac{x}{x+1} \tag{4.3.24}$$

This was e.g. the case in LEP [44].

Validity of HTGEN

The simulation of compton scattering is not included in PLACET-HTGEN, but the effect can be analytically estimated with the above formulas. Compton scattering becomes more relevant for high beam energies and is in most cases negligible for small energies.

4.3.3 Synchrotron Radiation

A relativistic particle following a bent trajectory looses energy due to synchrotron radiation. This can lead to an energy spread in the beam resulting in a generation of halo particles. E.g. in a quadrupole particles further away from the center of the quadrupole are focused more towards the center, so the orbit is more bent than the orbit of a particle closer to the center. A smaller bending radius implies a higher emitted synchrotron radiation power and with it a larger energy loss.

4.3.4 Residual Gas Ionization, Electron and Ion Cloud Effects

Electron Cloud Effects

Free electrons in the beampipe can be generated by the ionization of the residual gas or by synchrotron radiation photons, which hit the beampipe and knock out photo-electrons. If the beam particles are positively charged, the electrons are accelerated in the beam field and hit the wall of the beampipe. The wall then emits more electrons due to secondary emission. The electrons are again accelerated in the beam field and knock out more and more electrons of the wall. Hence in a circular accelerator, every time the beam passes, new electrons are generated and a significant number of electrons can be accumulated. The interaction of the beam with these electrons can then lead to an instability, known as *electron cloud effect*. Because new electrons are generated with each passage of the beam, the electron cloud effect is more relevant in storage rings than in linacs. In addition in a storage ring the number of photo-electrons is much higher than in a linear accelerator due to the high number of synchrotron radiation photons, which hit the beampipe.
Beams with negatively charged particles repell the electrons in the beampipe, so they are not accumulated around the orbit and usually don’t interact with the beam particles.

Validity of HTGEN

In summary electron cloud effects mostly occur in storage rings with a positively charged circulating beam and not in a electron accelerators.

Ionization of the Residual Gas

Electron beams ionize the residual gas in the beam pipe. The ionization cross section is given by [45]:

$$\sigma_{\text{ion}} = 4\pi \left(\frac{\hbar}{m_e c}\right)^2 \beta^2 \left[C_1 + C_2(2\ln(\beta\gamma) - 1)\right] \tag{4.3.25}$$

where C_1 and C_2 are characteristics of the molecules. Table 4.3.2 gives a list of values of C_1 and C_2 for different molecules together with the atomic number Z and the mass number A. Referring to [46] equation (4.3.25) is valid for relativistic velocities > 10 keV and has been experimentally approved by F. Rieke and W. Prepejchal for electrons of kinetic energies in the 1 MeV range [47].

Molecule	C_1	C_2	Z	A
H_2	8.1	0.5	2	2
N_2	34.8	3.7	14	28
CO	35.1	3.7	14	28
O_2	38.8	4.2	16	32
H_2O	32.3	3.2	10	18
CO_2	55.9	5.75	22	44

Table 4.3.2: C_1 and C_2 for different molecules

Each electron ionizes $n_{\mathrm{gas}}\sigma_{\mathrm{ion}}$ ions per unit length [48], hence the number of ions per unit length at the end of one bunch is:

$$\lambda_{\mathrm{ion}} = N n_{\mathrm{gas}} \sigma_{\mathrm{ion}} \tag{4.3.26}$$

and respectively at the end of one train:

$$\lambda_{\mathrm{ion}} = n N n_{\mathrm{gas}} \sigma_{\mathrm{ion}} \tag{4.3.27}$$

where n is the number of bunches per train, N the number of electrons per bunch and n_{gas} the residual gas density.
To get an estimate for the ionization of the residual gas, the line density as seen by the beam is compared with the maximal longitudinal ion density at the end of one train. The line density as seen by the beam is given by:

$$\lambda_{\mathrm{gas}} = A_{\mathrm{beam}} n_{\mathrm{gas}} \tag{4.3.28}$$

where A_{beam} is the beam cross section. The beam cross section is given by the area of the beam ellipse $\pi a_x a_y$ (fig. 4.3.4), whereas the semiaxis of the ellipse are related to the rms beam sizes by $a_{x,y} = \sqrt{5}\sigma_{x,y}$. If the residual gas consists of different molecules, the total longitudinal density is given by the sum of the longitudinal density of the residual gas constituents λ_i. The same holds for the number of ions per unit length at the end of one train/bunch.

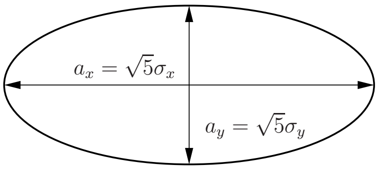

Figure 4.3.4: beam cross section

$$\lambda_{\mathrm{gas/ion}} = \sum_i \lambda_{i,\mathrm{gas/ion}} \tag{4.3.29}$$

We define the residual gas ionization by the ratio of the number of ions per unit length to the line density:

$$\text{Ionization} = \frac{\lambda_{\text{ion}}}{\lambda_{\text{gas}}} \tag{4.3.30}$$

Validity of HTGEN

In the present treatment, the residual gas is assumed to be neutral. A considerable ionization would imply changes in the halo generation, but for low energies the residual gas ionization is mostly irrelevant as the cross section increases with the beam energy (4.3.25). To assure the validity of HTGEN a rough estimate can always be obtained analytically.

Ion Cloud Effect - Conventional Ion Instability and Fast Ion Instability

Conventional Ion Instability:
The ion cloud effect mainly occurs in electron accelerators because a positively charged beam will typically push the ions to the wall of the vacuum chamber before they can do a significant damage to the beam. In the case of an electron beam the ions can be either lost between two bunches or they are not enough accelerated, so that they don't reach the wall before the next bunch arrives and get trapped. In the latter case the number of ions around the beam increases linearly with the number of bunches passing.
In circular machines when the gap between two bunches is not large enough to clear the ions from the chamber, the ions are trapped and the number of ions increases rapidly. This is known as the *conventional ion instability* (fig. 4.3.5). To avoid the ion trapping, a gap is introduced between the bunches/trains or clearing electrodes are used (fig. 4.3.6).

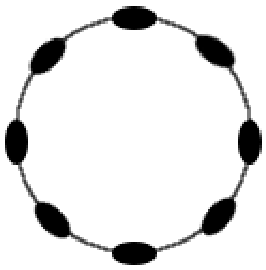

Figure 4.3.5: Conventional ion trapping, no gap in e^--beam, trapped ions, ion lifetime $\gg 1$ turn

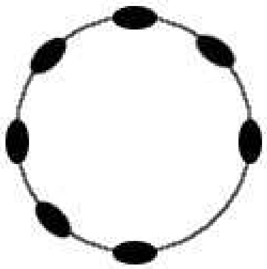

Figure 4.3.6: Fast ion instability, gap in e^--beam, ions not trapped, ion lifetime < 1 turn

Fast Ion Instability:
Even if the ion lifetime is smaller than one turn, they can still lead to an instability, the *fast ion instability*. The fast ion instability is a head-tail effect, where the trains/bunches in the head built up an ion cloud, which then interacts with the bunches/trains in the tail

while the ones in the head are not affected (fig. 4.3.7). Therefore it can arise in circular machines as well as in linacs. In the following we will shortly introduce the relevant parameters necessary for our rough estimates.

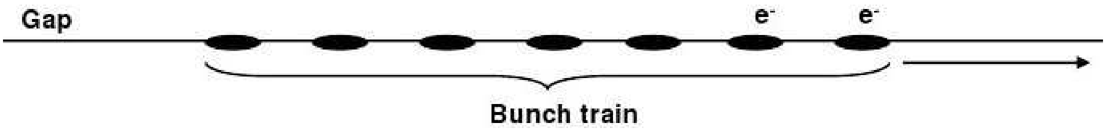

Figure 4.3.7: The fast beam ion instability is a head tail effect.

The electrons from the ionized molecules are repelled by the negatively charged bunch and gain high enough velocities to reach the wall before the next bunch arrives. Because the ions are heavier than the electrons their transverse velocity can be so small, that they move less than the transverse beamsize before the next bunch arrives and hence affect the following bunch. The resultant vertical motion of the beam particles and the ions is a mutually driven oscillation. The ions can be trapped between bunches/trains if their coherent transverse frequency f_i is smaller than the frequency of the arriving bunches/trains [49]:

$$4f_i < \frac{c}{\Delta z} \tag{4.3.31}$$

where Δz is the distance between two bunches/trains. This trapping condition is derived from the assumption that the ions only move very little between the passage of consecutive bunches. There exist different trapping conditions, but all have the form of $\mathrm{const} \cdot \mathrm{f_i} < \mathrm{c}/\Delta\mathrm{z}$, where the constant const lies between 3 and 4 [49], [50].
The oscillation frequency f_i is given by [50]:

$$f_i \approx \frac{c}{\pi}\sqrt{\frac{Q_i \tilde{n} r_p}{3\sigma_y(\sigma_x+\sigma_y)\Delta z A}} \tag{4.3.32}$$

r_p is the classical proton radius, A the atomic weight, $\sigma_{x/y}$ the horizontal/vertical rms beam size, Q_i the ion charge and $\tilde{n}$ the number of particles per bunch $\tilde{n} = N$ (or in the case of trapping between trains $\tilde{n} = nN$). With this expression of the oscillation frequency (4.3.32), inequality (4.3.31) can also be written as a lower limit to the mass number A:

$$A > A_{\text{trap}} = \frac{16 Q_i r_p \tilde{n} \Delta z}{3\pi^2(\sigma_x+\sigma_y)\sigma_y} \tag{4.3.33}$$

Ions with a mass number smaller than A_{trap} are therefore not trapped, while all with a higher mass number are trapped.
For the three studied accelerators only trapping between bunches can occur and we will assume from now on, that the ions are only trapped between the bunches and not between trains. If the coherent oscillation of the ions is small compared to the beam size, the force

acting from the ions on the beam can be assumed to be linear. Otherwise the decay of the force at large distances would have to be considered. Under this condition an initial vertical perturbation $\hat{y}$ would increase purely exponentially [49]

$$y_b \sim e^{\sqrt{t/\tau_e}} \tag{4.3.34}$$

with an e-folding risetime of [51]:

$$\frac{1}{\tau_e} = \frac{\lambda_{ion} r_e c}{\sqrt{18} a \sqrt{Q_i} \left(\sqrt{\epsilon_y \epsilon_x \beta_x / \beta_y} + \epsilon_y \right)} \tag{4.3.35}$$

where f_i is the coherent ion oscillation frequency given by (4.3.32). The parameter a is the peak-to-peak ion-frequency variation and takes the variation of the ion frequency along the beam line as well as the ion decoherence, e.g. caused by the dependence of the vertical ion oscillation frequency on the horizontal position into account. For a FODO lattice $a \approx 0.1$. In [52] it is shown that (4.3.35) underestimates the risetime by a factor 2-3.

Another important parameter for the relevance of the fast-ion instability is the number of risetimes n_{rt} the beam needs to pass the beamline and the coherent and incoherent tune shift $\Delta\nu_{x,y,\mathrm{coh,incoh}}$ induced by the fast ion instability [53].

$$n_{rt} = L/(c\tau_e) \tag{4.3.36}$$

where L is the length of the beamline.

$$\begin{aligned} \Delta\nu_{x,y,\mathrm{incoh}} &= \frac{\beta_{x,y} r_e Q_i \lambda_{\mathrm{ion}} L}{4\pi\gamma\sigma_{x,y}(\sigma_x + \sigma_y)} \\ \Delta\nu_{x,y,\mathrm{coh}} &= 2\Delta\nu_{x,y,\mathrm{incoh}} \end{aligned} \tag{4.3.37}$$

To avoid an instability the caused tune shift and the number of risetimes should stay < 1.

Validity of HTGEN

The fast ion instability can not yet be simulated by PLACET, but it is planed to include the fast ion instability simulation code FASTION [54] into PLACET.

4.3.5 Touschek Effect and Intrabeam Scattering

By coulomb scattering the typically small transverse momentum of two beam particle can be transformed into a large longitudinal momentum. Both scattered particles are lost, one with too much and one with too little momentum. This effect is known as *Touschek effect*. *Intrabeam Scattering* is the multiple coulomb scattering effect and leads to diffusion in all three directions and a change in the beam dimensions. Both effects are only relevant for low energy beams with a very small beam size. The particle beams we studied have all a relatively large beam size and we don't expect any halo and tail generation due to intrabeam scattering or Touschek effect. Analytical estimates can be obtained e.g. by the formulas derived by Piwinski [55].

Validity of HTGEN

For small beam energies and small beam sizes Touschek effect and intrabeam scattering become relevant and the simulation would have to be extended for a realistic halo and tail simulation. The Touschek effect could be relatively easy implemented in HTGEN. One possibility is shown in [56], but in the case of HTGEN it would be probably easier to implement the cross section and angle distribution analogically to mott scattering and bremsstrahlung.

4.3.6 Space Charge Effect

The particle motion depends not only on the external fields, but also on the fields from the coulomb interactions between the particles themselves. The effect of the coulomb forces can be separated into two contributions. First the space charge field, which is the smoothened field resulting from the combination of the fields of all particles. Second the short range fields from binary coulomb collisions. According to [2] the short range fields are very small compared to the average space charge field.

The electric and magnetic self field of the beam can be calculated using the Maxwell equation and depend on the beam distribution. These fields exert a force on a test particle with charge q and coordinates x, y and z given by the Lorentz force:

$$\vec{F} = q\left(\vec{E} + \vec{v} \times \vec{B}\right) \tag{4.3.38}$$

As shown in [2] the transverse electric force acts repulsive on the particles while the transverse magnetic force has an attractive effect and tends to compensate for the defocusing electric force with increasing beam velocity. When the velocity approaches the speed of light the electric and magnetic self field tend cancel themselves in the transverse plane. The longitudinal motion is only affected by the electric self field and scales with $1/\gamma^3$. In linear accelerators the longitudinal electric self field always has a defocusing effect, while in circular accelerators it is defocusing below transition and focusing above.

For a three dimensional uniform ellipsoidal beam the electric field is given by [2]:

$$\begin{aligned} E_{sx} &= \frac{3qN\left(1-f\right)}{4\pi\epsilon_0\left(a_x+a_y\right)a_z}\frac{x}{a_x}, \quad E_{sy} = \frac{3qN\left(1-f\right)}{4\pi\epsilon_0\left(a_x+a_y\right)a_z}\frac{y}{a_y} \\ E_{sz} &= \frac{3qN\left(1-f\right)}{4\pi\epsilon_0 a_x a_y}\frac{z}{a_z} \end{aligned} \tag{4.3.39}$$

where a_x, a_y and a_z are the semiaxis of the ellipsoid in the laboratory frame, N the number of particles per bunch and q the charge of one particle. The semiaxis are related with the rms beam sizes by $a_{x,y,z} = \sqrt{5}\sigma_{x,y,z}$. x, y and z are the coordinates of the test particle relative to the bunch centroid. The quantity f is an ellipsoidal form factor and is a function of the parameter $p = \gamma a_z/\sqrt{a_x a_y}$ with $f(0) = 0$. Values for $f(p)$ can be found in [2]. For the three studied accelerators $p \approx 0$ and therefore $f = 0$.
In the transverse plane the equation of motion without space charge effects is given by the Hill's equation (1.2.3). The effect of space charge is included by adding a space charge term F_s, which includes the self electric as well as the self magnetic forces [2]:

$$x'' + k(s)x - \tilde{F}_{sc} = 0 \tag{4.3.40}$$

$\tilde{F}_s$ is the space charge force term and is related to the electric field by

$$\tilde{F}_{sc} = \frac{qE_s}{\gamma^3\beta^2 m_0 c^2} \tag{4.3.41}$$

where γ and β are the relativistic γ and β factor, m_0 the rest mass of one beam particle and c the speed of light. In general the space charge term is not linear in x, but in the case of an elliptical bunched beam the electric field is linear in all three directions and eq. (4.3.40) can be simplified:

$$x'' + (k(s) - F_{sc})x = 0 \tag{4.3.42}$$

where $F_{sc} = \tilde{F}_{sc}/x > 0$. In the case of a FODO lattice $k(s)$ is the quadrupole focusing strength, which is related to the average β-function by

$$k(s) = \frac{1}{\langle\beta\rangle^2} \tag{4.3.43}$$

Eq. (4.3.42) yields, that the focusing strength of the quadrupole is reduced by the effect of the space charge force.

Longitudinal Beam dynamics with Space Charge

A linear accelerator is normally operated below Transition, i.e. on the rising edge of the rf wave, so that a longitudinal focusing is achieved by the rf acceleration [2]. This description is not adequate for the CLIC decelerator neither for TBONE.

In the decelerator the particles experience only a defocusing effect caused by the wakefields. The influence of space charge could be estimated by comparing the self electric longitudinal field given by eq. (4.3.39) with the longitudinal field in the PETS.
In the case of TBONE, a large energy spread is desired before the bunch compressor. Therefore all three cavities are operated above transition and enforce the longitudinal defocusing forces (ch. 4.4.3) instead of reducing them. Also in this case, a rough estimate could be obtained by the comparison of the longitudinal space charge to the longitudinal field in the cavities.
The calculation of the longitudinal electrical field in cavities and PETS is not trivial and therefore we will confine ourselves to the transverse space charge effects. In general space charge effects are only relevant for electron beams in the keV range and we suspect that the longitudinal space charge effects can be neglected.

Validity of HTGEN

Space charge effects are not included in PLACET-HTGEN, but are normally only relevant for electron beams in the keV range. For an estimate of the relevance of space charge effects the formulas presented above can be used.

4.3.7 Beam Loading and Wakefields

Only for very low energies in the keV range electrons can't be treated anymore as relativistic particles. Even in low energy accelerators, the beam energy lies in the MeV range and we can assume that the beam particles are relativistic and move approximately with the speed of light.
A free relativistic charged particle emits radiation perpendicular to its direction of motion with a narrow angular spread of $1/\gamma$ and the longitudinal electric field approaches zero. This is still the case for a relativistic particle moving in a perfectly conducting pipe. When the fields traveling along with the relativistic particle encounter geometric variations such as rf cavities, kickers, diagnostic components etc., they are scattered on the structure and can act back on the beam. As the velocity of the particles is close to the speed of light the principle of causality prohibits that the radiation catches up with the source particles or particles in front, but it can act back on trailing particles. Therefore the scattered radiation carried along with every beam particle is called the *wakefield* of the particle.
For short bunches the energy of the wakefields tends to increase, because of the constructive interference of the radiation from different sources. At lower velocities the wakefield of the beam becomes more isotropic and destructive interference reduces the energy of the wakefields. For even lower energies the effect of the wakefields is normally much smaller than the effect of the direct space charge fields.

Wakefields are generally damped oscillatory electromagnetic waves, which can be described as a sum of all resonant modes excited in the structure. The wakefield effect of the main accelerating mode is also called *beamloading* and is commonly stronger than the effect of the higher order modes. Modes with frequencies higher than the cut off frequency of the structure propagate away along the beam pipe and do not stay localized, while modes with frequencies below the cutoff frequency remain localized in the structure and may effect trailing bunches.

One distinguishes between *short-range* and *long-range* wakefields. The short-range wakefields, which are generated by the particles in the head of the bunch, affect trailing particles in the same bunch, leading to energy loss and a transverse deflection of off-axis particles. The long-range wakefields influence trailing bunches. The high-Q transverse modes of the long-range fields have the strongest effect and cause time varying transverse deflection of trailing bunches.

Validity of HTGEN

For the CLIC PETS in combination with the drive and the TESLA cavities in combination with the ILC main beam the wakefields have been calculated with GdFidl and/or other tools and are included in PLACET. For other beams and elements the simulation code would have to be extended. For electron beams in the MeV to GeV range wakefields can have a considerable effect on the beam dynamics as seen on the example of the TBL drive beam and have to be taken into account.

4.3.8 Optics Related Effects

The relevance of optics related effects do more depend on the beam size and energy spread than the average beam energy. Therefore they are not more or less relevant for low energy beams.

4.3.9 Various Other

Dark currents and noise and vibrations are not energy dependent and have to be included if a considerable effect on the beam is expected.

4.4 Analytical Estimates and Simulation Results

We have performed halo and tail generation studies for three accelerators: the CLIC decelerator, the CTF3 TBL and TBONE. All input parameters for the CLIC decelerator and

CTF3 are summarized for a better overview in appendix C. Parameters of importance for scattering processes are defined in appendix appendix B.

4.4.1 CLIC Drive Beam Decelerator

The CLIC drive beam decelerator is the rf power source of the main linacs (chapter 2.1). To ensure a uniform power supply, it is essential to transport the drive beam with very few losses until the end of the decelerator. Beside the direct effect on the rf power production, lost beam or halo particles or emitted radiation could considerably increase the heatload of the PETS and cause rf breakdown. The results of the halo and tail generation studies for the decelerator were published in [57].

Analytical Estimates and Simulation Results

All decelerators have a slightly different length depending on the corresponding lattice of the main linac. We expect the largest halo generation for the longest decelerator, for which we performed the simulations. As a model we use the baseline specification of the decelerator, which includes the effect of a beam offset, misalignment and longitudinal as well as transverse wakefield effects. We chose a sliced beam model with 200 bunches per train, 51 slices and 1 macroparticle per slice.

The residual gas in the decelerator consists of 40% $\mathrm{H_2O}$, 40% $\mathrm{H_2}$ and the remaining 20% shared among $\mathrm{CO}, \mathrm{N_2}, \mathrm{CO_2}$ with a total pressure of 10 nTorr and a temperature of 300 K, which we also used for the analytical estimates. For the simulations we used for simplicity a gas equivalent of pure $\mathrm{N_2}$ gas.

The basic parameters for the CLIC drive beam decelerator are given in table 4.4.1 and 4.4.2. The input parameters of the different halo sources are listed in the belonging section. All input parameters are summarized together with the CTF3 input parameters in appendix C.

pressure [nTorr]	10
temperature [K]	300
molecule density $[\mathrm{m}^{-3}]$	3.22×10^{14}

Table 4.4.1: CLIC vacuum specifications

Wakefields:

The PETS dipole mode transverse wakefields and fundamental mode longitudinal wake field is included in the simulation and the results presented in [12]. A summary of the results is given in ch. 2.3.3.

DB station length $[\mathrm{m}]$	1053.23
number of trains	1
Bunches per train	2928
Bunch separation $[\mathrm{m}]$	0.025
Bunch length $[\mathrm{mm}]$	1
number of particles per bunch $[10^9]$	52.5
E_{initial} $[\mathrm{GeV}]$	2.4
E_{final} $[\mathrm{GeV}]$	0.4

Table 4.4.2: Beam and Lattice Parameters of the CLIC Drive Beam Decelerator

Misalignment and Beam offset:
The effect of misalignment of quadrupoles and PETS is described in detail in [58].
As the strength of the dipole wake of the PETS is proportional to the offset of the source particle, the caused transverse kicks will grow linearly with the transverse misalignment. A small angle error in the orientation of the PETS has the same effect as a position offset and can therefore be simulated as latter. In order to avoid large kicks and a resulting envelope growth, the PETS misalignment must be kept below an rms offset of $200\ \mu\mathrm{m}$. In the performed simulation the misalignment error is set to the maximum value of $200\ \mu\mathrm{m}$.
A quadrupole offset will add a dipole component in the lattice, resulting in transverse kicks. The quadrupoles and BPMs (Beam Position Monitors) can be pre-aligned at best to an accuracy of $20\ \mu\mathrm{m}$. An offset of this magnitude would increase the beam envelope unacceptably. The misalignment of the quadrupoles can be compensated by correction schemes like DFS (Dispersion Free Steering). We haven't included the correction of dispersion free steering in the simulation and therefore used a reduced misalignment of the quadrupoles of $2\ \mu\mathrm{m}$.
An offset of the beam has in principle the same effect as a misalignment of the elements. For the simulations we have assumed an initial beam offset equal to the corresponding rms beam size. The beam sizes and beam divergences are given in table 4.4.3.

Initial rms beam size in x $[\mathrm{mm}]$	0.14
Initial rms beam size in y $[\mathrm{mm}]$	0.33
Initial beam divergence in x' $[\mathrm{mrad}]$	0.23
Initial beam divergence in y' $[\mathrm{mrad}]$	0.10

Table 4.4.3: Beam Size Parameters of the CLIC Drive Beam

Dispersion:
In the definition of the dispersion function a small momentum spread of the beam is assumed ch. 1.2.3. This assumption doesn't hold any more for the decelerator as the particle

energy can differ significantly from the reference energy . In general we could extend the definition and define the dispersion function over the taylor expansion of the particle trajectory $x(s,p+\Delta p)$ with a sufficient large Δp. A better approach taken in [12] is to inspect the behaviour of an energy dependent beta function $\beta(s,E(s))$. In [12] it is shown that the low energy particles are responsible for the envelope growth.

Beam Gas Scattering:

The total number of halo particles N_{halo} at the end of the decelerator due to beam gas scattering is given by the integrated scattering fraction multiplied by the total number of beam particles:

$$N_{\text{halo}} = n\ N\ S_{\text{int}} \overset{(\text{B.0.5})}{=} n\ N \sum_{i=1}^{\text{tot. numb. of elements}} P_i\ l_i \tag{4.4.1}$$

where N is the number of particles per bunch, n the number of bunches per train, P_i the scattering probability in the element i and l_i the length of the element. As the residual gas consists of different constituents (40% $\mathrm{H_2O}$, 40% $\mathrm{H_2}$ and the remaining 20% shared equally among $\mathrm{CO}, \mathrm{N_2}, \mathrm{CO_2}$, so $20/3\%$ each), the scattering probability P_i is the sum over the scattering probabilities of the constituents j with a density n_j (table 4.4.6)

$$P_i = P_{i,\text{brem}} + P_{i,\text{mott}} = \sum_{j=1}^{\text{numb. of resid. gas constit.}} n_j(\sigma_{i,j,\text{brem}} + \sigma_{i,j,\text{mott}}) \tag{4.4.2}$$

where $\sigma_{i,j,\text{mott/brem}}$ is the mott respectively bremsstrahlung cross section of the constituent j in the element i given by eq. (4.3.4), (4.3.10) and (4.3.13). The mott scattering cross section depends on the particle energy and the minimal scattering angle, which we approximated by the beam energy defined as the energy of the central slice and the beam divergence given by eq. (4.3.6) in the element. As twiss parameters and emittance in each element we took the simulated values which correspond to the beam size definition of the twiss parameters and emittance. The bremsstrahlung cross section only depends on the minimal photon energy, which we set to a fixed value of $k_{\text{min}} = 0.01$. Using these input parameters the integrated scattering fraction and the total number of haloparticles for the individual process as well as the total values yield to the values in table 4.4.4. The total integrated scattering fraction S_{tot} is very small and we therefore expect a very small halo generation due to beam gas scattering.

Even if we don't expect a significant halo generation, we want to analyze the obtained tracking results to point out some characteristics of halo and tail generation.

A comparison of the scattering fraction of bremsstrahlung and mott scattering shows, that mott scattering is the dominant process. As the mott scattering cross section increases with decreasing energy, the halo generation due to mott scattering is stronger in the end

$S_{\mathrm{mott,tot}}$	7.69×10^{-9}
$S_{\mathrm{brem,tot}}$	1.17×10^{-10}
S_{tot}	7.81×10^{-9}
N_{halo}	1.20×10^{6}

Table 4.4.4: Integrated scattering fraction along the decelerator for mott scattering $S_{\mathrm{mott,tot}}$ and bremsstrahlung $S_{\mathrm{brem,tot}}$

of the decelerator than at injection, which is clarified by the initial and final scattering probability (table 4.4.5). Bremsstrahlung is energy independent and stays constant along the whole beamline (table 4.4.5). The analytical estimates enable the computation of the total number of halo particles, but not the halo distribution and the number of lost particles as well as their characteristics, which we therefore simulated with PLACET-HTGEN. For simplicity we used a gas equivalent of N_2 instead of the exact residual gas constitution, a constant scattering angle equal to the minimal beam divergence of $97.58\ \mu\mathrm{rad}$ along the decelerator and a constant minimal photon energy of $k_{\mathrm{min}} = 0.01$. In fig. 4.4.1 and fig. 4.4.2 the trajectory of beam and halo particles along the whole decelerator and for closer inspection an extract of the decelerator is shown. Halo particles, which are scattered far outside the beam core follow a trajectory far away from the beam core and finally get lost, when the trajectory increases too much.

$P_{\mathrm{mott,initial}}\ \mathrm{m}^{-1}$	7.85×10^{-12}
$P_{\mathrm{mott,final}}\ \mathrm{m}^{-1}$	4.19×10^{-11}
$P_{\mathrm{brem,initial}}\ \mathrm{m}^{-1}$	1.11×10^{-13}
$P_{\mathrm{brem,final}}\ \mathrm{m}^{-1}$	1.11×10^{-13}

Table 4.4.5: Initial and final scattering probability for mott scattering and bremsstrahlung. The effect of mott scattering increases along the decelerator while bremsstrahlung stays constant.

Especially interesting in the decelerator is the energy distribution of the lost halo particles. Most halo particles get lost at the end of the decelerator and have mainly a low energy (fig. 4.4.3). This agrees with the results obtained in [12], where especially the most decelerated particles are responsible for the envelope growth in the decelerator .

Typically halo particles with a large initial scattering angle get lost. This effect can also be seen in the decelerator.perhaps an additional pictures with the scattering angle of the lost halo particles

In total a fraction (the ratio between the number of lost particles and the total number of beam particles) of 2.35×10^{-6} get lost. Hence the losses due to beam gas scattering in the decelerator are very small and not of importance.

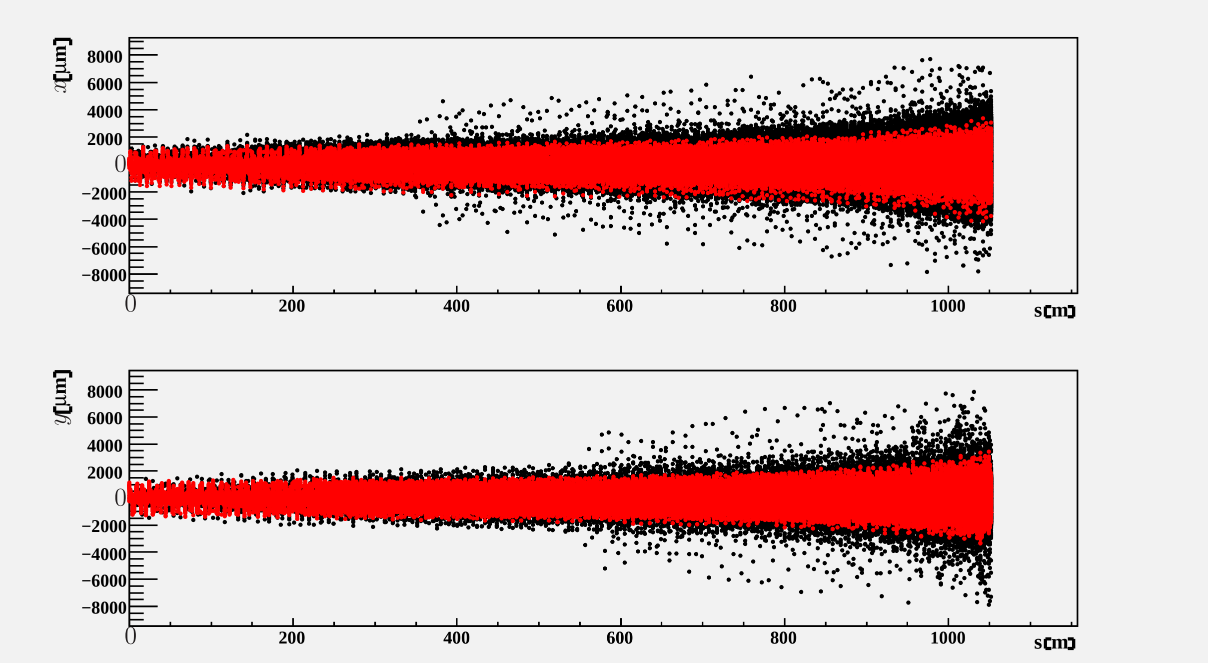

Figure 4.4.1: Tracking of halo and beam along the longest CLIC decelerator: due to the deceleration the beam emittance increases along the whole decelerator.

Discussion and Analytical Estimates of Halo and Tail Generation Sources not Included in the Simulation

Ionization of the Residual Gas:
To estimate the ionization of the residual gas, we used a residual gas constitution of 40% $\mathrm{H_2O}$, 40% $\mathrm{H_2}$ and the remaining 20% shared equally among $\mathrm{CO}, \mathrm{N_2}, \mathrm{CO_2}$, so $20/3\%$ each. As the ionization cross section increases with the beam energy, a upper limit for the residual gas ionization is the ionization at the end of the drive beam, which is equivalent to the end of one train as the drive beam consists of only one train, and the maximal beam energy, which is the initial beam energy of $2.4\ \mathrm{GeV}$. For the calculation we used eq. (4.3.25), (4.3.27), (4.3.28) and (4.3.30). The residual gas densities and beam sizes are given in table 4.4.2,table 4.4.6 and table 4.4.7 and the results in table 4.4.8. For $\mathrm{CO_2}$ the ionization is largest but is still very small with 6.1%. The total ionization of the residual gas is with 1.8% also very small and won't have any influence on the halo and tail generation.

Compton Scattering:
Assuming a temperature of $300\ \mathrm{K}$, we obtain using eq. (4.3.18) and (4.3.19) a photon density of $5.45 \times 10^{14}\ \mathrm{m}^{-3}$ and an average photon energy of $0.07\ \mathrm{eV}$. As the dimensionless parameter x defined in eq. (4.3.21) stays below 10^{-3}, we used eq. (4.3.22) for the calculation of the compton cross section. Therewith the integrated scattering probability

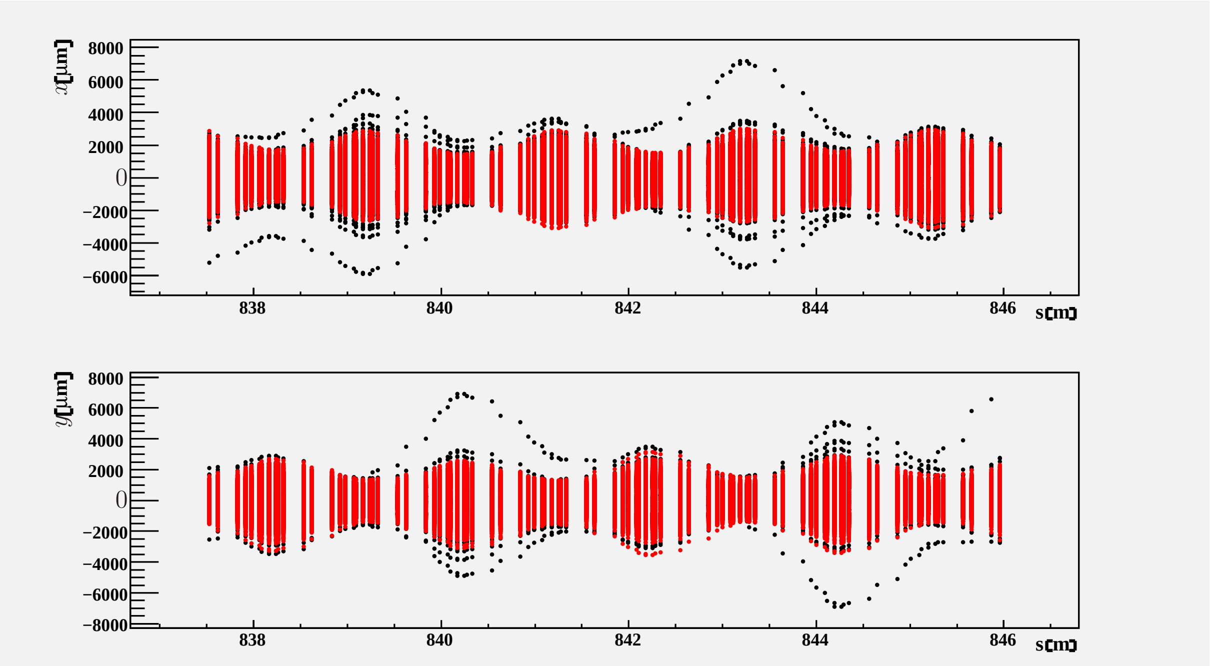

Figure 4.4.2: Tracking of halo and beam along and extract of the longest CLIC decelerator: the amplitude of some halo particles has increased significantly and the particle will soon be lost due to overfocusing in a quadrupole.

	$\rho_{\mathrm{gas}}[\mathrm{m}^{-3}]$
H_2O	1.29×10^{14}
H_2	1.29×10^{14}
N_2, CO, CO_2	6.44×10^{13}

Table 4.4.6: Molecule Density

$\sigma_{x,\mathrm{initial}}$ [mm]	0.14
$\sigma_{y,\mathrm{initial}}$ [mm]	0.33
$\sigma_{x,\mathrm{final}}$ [mm]	1.50
$\sigma_{y,\mathrm{final}}$ [mm]	1.71
$\sigma_{x',\mathrm{initial}}$ [mrad]	0.23
$\sigma_{y',\mathrm{initial}}$ [mrad]	0.10
$\sigma_{x',\mathrm{final}}$ [mrad]	0.30
$\sigma_{y',\mathrm{final}}$ [mrad]	0.25
$\sigma_{z,\mathrm{initial}}$ [mm]	1.0
$\sigma_{z,\mathrm{final}}$ [mm]	1.0

Table 4.4.7: Initial and final rms beam sizes of the CLIC drive beam

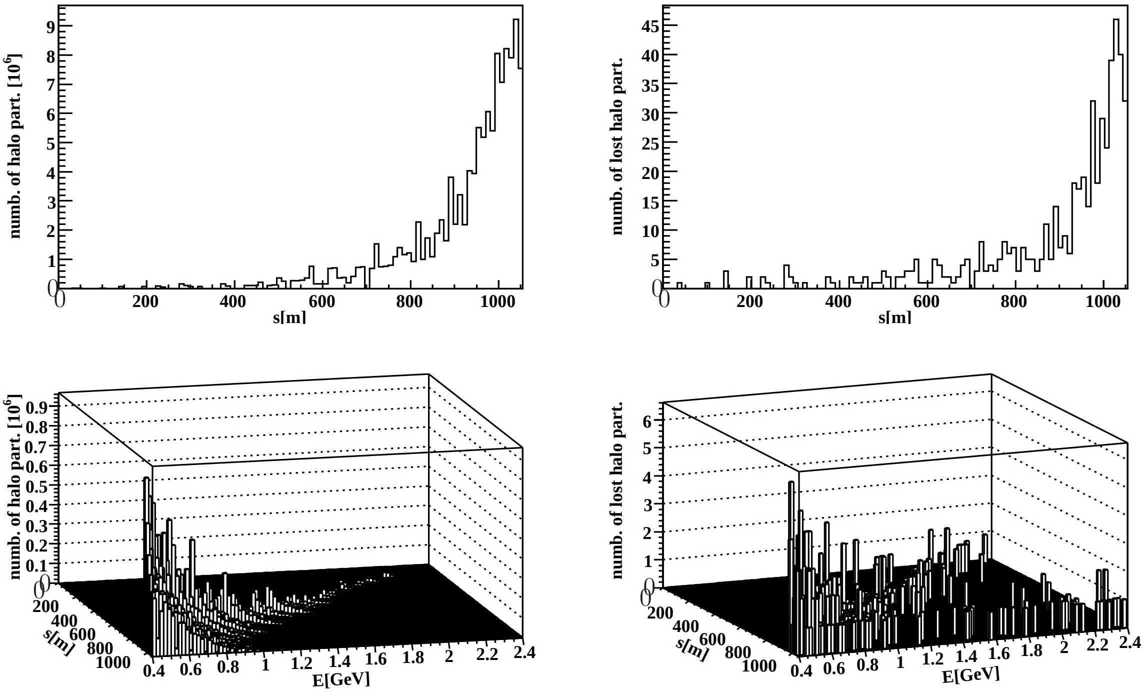

Figure 4.4.3: in the left upper corner: number of halo particles along the decelerator. in the right upper corner: number of lost particles along the decelerator. in the left down corner: energy distribution of the halo particles along the decelerator. in the right down corner: energy distribution of the lost halo particles along the decelerator

	σ_{ion} [barn]	$\lambda_{\text{ion}}[\text{m}^{-1}]$	$\lambda_{\text{gas}}[\text{m}^{-1}]$	gas ionization [%]
H_2O	1.56×10^6	3.09×10^6	1.62×10^8	3.4
H_2	3.01×10^5	5.96×10^5	1.62×10^8	0.7
CO	1.76×10^6	1.74×10^6	8.10×10^7	3.9
N_2	1.76×10^6	1.74×10^6	8.10×10^7	3.9
CO_2	2.77×10^6	2.74×10^6	8.10×10^7	6.1
total	-	5.76×10^6	3.15×10^9	1.8

Table 4.4.8: Residual gas ionization in the CLIC decelerator: A constant beam energy of 2.4 GeV is assumed. The given values refer to the values at the end of one train.

yields 3.82×10^{-11}, which is very small compared to mott scattering with an integrated scattering probability of 7.69×10^{-9}. Thus the effect of transverse deflection by compton scattering can be neglected. The energy spread caused by compton scattering is given by eq. (4.3.24) and lies between 0.04% at the end of the decelerator and 0.26% at injection. This is negligible compared to the energy spread induced by the transverse wakefields.

Synchrotron Radiation:
In the decelerator the energy loss due to synchrotron radiation is very small as the decelerator is a linear accelerator and the only significant energy loss due to synchrotron radiation could occur in the quadrupoles. In addition the small deceleration of the beam particles caused by the emission of synchrotron radiation photons is negligible compared to the deceleration experienced in the PETS.

Electron Cloud Effects:
As described in ch. 4.3.4 the electron cloud effect is not relevant in our case as the drive beam is an electron beam and the decelerator a linear beamline.

Ion Cloud Effects:
According to ch. 4.3.4 the conventional ion instability can not occur in the decelerator, because the decelerator is a linear beamline. A simulation of a possible fast-ion instability in the decelerator is planed but the implementation of the FASTION code [54] into PLACET is not yet completed. For an analytical estimate we follow the approach taken in ch. 4.3.4 which was also taken for the long transfer line of CLIC [59].
The number of rise times and the tune shift depend on the beam energy and the twiss parameters, which change considerably along the decelerator. To estimate the relevance of the fast-ion instability we calculated the critical parameters for the initial beam energy and twiss parameters as well as for the final ones.

As the drive beam consists of only one train, we can exclude trapping between trains.

Initial norm. emittance in x $[\mu\mathrm{m}]$	150.0
Initial norm. emittance in y $[\mu\mathrm{m}]$	150.0
Final norm. emittance in x $[\mu\mathrm{m}]$	351.4
Final norm. emittance in y $[\mu\mathrm{m}]$	340.0
Initial β-function in x $[\mathrm{m}]$	0.579
Initial β-function in y $[\mathrm{m}]$	3.354
Final β-function in x $[\mathrm{m}]$	5.029
Final β-function in y $[\mathrm{m}]$	6.778

Table 4.4.9: Initial and final emittance and β-function of the central slice.

The twiss parameters were obtained from the simulations and are listed in table 4.4.2, table 4.4.8, table 4.4.7, table 4.4.9. With an ion charge of $Q_i = 1$ we obtain a critical mass number defined by eq. 4.3.33 of $A_{\text{trap}} = 7.18 \times 10^{-3}$ for the initial values and $A_{\text{trap}} = 1.97 \times 10^{-4}$ for the final values. Only ions with a mass number bigger than the critical mass number get trapped, which are all in our case. The number of risetimes n_{rt} and the incoherent tune shift $\Delta\nu$ given by eq. 4.3.36 and 4.3.28 yields: The tune shift

$\Delta\nu_{x,\text{initial}}$	5.3×10^{-3}
$\Delta\nu_{y,\text{initial}}$	1.3×10^{-2}
$\Delta\nu_{x,\text{final}}$	1.6×10^{-2}
$\Delta\nu_{y,\text{final}}$	3.7×10^{-3}

Table 4.4.10: Incoherent Tune Shift due to the Fast-Ion Instability

$[n_{rt,\text{initial}}, 3n_{\text{rt,initial}}]$	$[1.89, 5.69]$
$[n_{rt,\text{final}}, 3n_{\text{rt,final}}]$	$[0.54, 1.64]$

Table 4.4.11: Number of Rise Times of the Fast-Ion Instability

stays below 1 but the number of rise times is bigger than 1 which indicates a possible occurance of the fast-ion instability. If the fast-ion instability could occur in the decelerator will be shown by the planned simulations.

Touschek Effect and Intrabeam Scattering:

We would expect that intrabeam scattering and Touschek effect are not relevant in the decelerator as the beam size is quite large and the energy still relatively high. On the other hand Touschek effect and intrabeam scattering could be more important in the CLIC decelerator than in comparable linear accelerators without decelerating sections as beam particles, which have lost longitudinal momentum due to coulomb interact ion, could lose almost all their longitudinal momentum during the deceleration and get lost [56], [60]. Both effects are not implemented in the simulation and a particle loss due to Touschek effect combined with the deceleration can only be simulated.

Space Charge Effect:

The decelerator is a sequence of FODO cells, where the strength of the quadrupoles can vary according to the beam energy. For a rough estimate we followed ch. 4.3.6 to obtain the ratio between the space charge force F_sc and the focusing strength k. The necessary input parameters are listed in table 4.4.2 and table 4.4.7.

$\langle\beta_{x,\text{initial}}\rangle$ m	0.58
$\langle\beta_{y,\text{initial}}\rangle$ [m]	3.35
$\langle\beta_{x,\text{final}}\rangle$ [m]	1.13
$\langle\beta_{y,\text{final}}\rangle$ [m]	3.38

Table 4.4.12: initial and final average β-function over all slices

The quadrupole focusing strength k was calculated from the average beta function over all slices $k = 1/\langle\beta\rangle^2$ (table 4.4.7). All ratios stay below 0.1% (table 4.4.13), which is very small and we conclude, that the effect of the transverse space charge is negligible.

$F_{sc,x,\text{initial}}/k_{x,\text{initial}}$ [%]	2.04×10^{-4}
$F_{sc,y,\text{initial}}/k_{y,\text{initial}}$ [%]	1.42×10^{-2}
$F_{sc,x,\text{final}}/k_{x,\text{final}}$ [%]	2.17×10^{-3}
$F_{sc,y,\text{final}}/k_{y,\text{final}}$ [%]	8.54×10^{-2}

Table 4.4.13: Ratio between the space charge forceF_{sc} and the focusing strength k

Mismatch:
Studies have shown, that a mismatch of even a few percent doesn't have an effect on the beam envelope. Therefore if the beam is not heavily mismatched, we don't expect an additional halo generation from this source [61].

Coupling:
In the baseline specification of the drive beam decelerator coupling is not included. For quadrupoles and PETS it is a good assumption that the motion in the transverse plane is uncoupled. The effect of coupling due to misalignment has been studied in [58] and shows a rotation of the quadrupoles by less than $1\ \mathrm{mrad}$ changes the beam envelope only insignificantly.

Nonlinearities:
As in the PETS simulation only the dipole wake is included and no field errors are defined for the quadrupoles, our simulations are purely linear. The error from higher order modes of the PETS has not yet been studied, but small field errors of the quadrupoles won't probably lead to a significantly different behaviour of the beam [61].

4.4.2 CTF3 TBL Drive Beam

4.4.3 TBONE

We have studied halo and tail generation only for the superconducting linac of TBONE, where the beam is accelerated to an energy of $87\ \mathrm{MeV}$. The simulation for TBONE have just started and therefore many effects are not yet implemented and the tracking is not totally adapted to the special case of TBONE. However the performed simulation give a rough estimate of the halo and tail generation in TBONE. As TBONE is supposed to deliver high power coherent THz radiation, the beam has to be transported with minimal losses in order to assure the required radiation power. Therefore an estimate of losses due to halo and tail generation is needed.

Analytical Estimates and Simulation Results

For the simulation and analytical estimates we assumed that the residual gas would consist to $100\ \%$ of H_2 with a total pressure of $0.07\ \mathrm{nTorr}$ and a temperature of $2\ \mathrm{K}$. We have simulated the beam dynamics with PLACET, which is described in ch. 3.2. The beam parameters and vacuum specification are given in table 4.4.14 and 4.4.15.

pressure [nTorr]	0.075
temperature [K]	2
molecule density $[\mathrm{m}^{-3}]$	3.62×10^{14}

Table 4.4.14: TBONE vacuum specifications

superconducting linac length $[\mathrm{m}]$	3.11
number of bunches	1
number of particles per bunch $[10^9]$	0.52
Bunch length $[\mathrm{mm}]$	0.62
$E_{\text{initial}}\ [\mathrm{MeV}]$	8.35
$E_{\text{final}}\ [\mathrm{MeV}]$	87.02

Table 4.4.15: Beam and Lattice Parameters of TBONE

Wakefields:

For the wakefield mode calculation we used the routine written for the ILC main linac with changed bunch length and charge. With this computation combined with PLACET, the longitudinal short and long range wakefields and the transverse dipole mode wakefield are included in the simulation [62]. In the case of TBONE the long range wakefields are not relevant as the TBONE beam only consists of one bunch. As the wakefields mainly depend on the geometry of the structure, the bunch charge, energy and length only an estimate of the wakefield effects can be obtained by the simulations. An exact computation of the wakefields could be performed with [22]. The results of the simulations are shown in ch. 3.2.

Beam Gas Scattering:

The method of beam gas scattering simulations is described in detail in ch. 4.4.1 and we therefore only present the obtained results. As emittance, β-function and beam energy we used the values obtained by the simulation with PLACET. The integrated scattering fraction and total number of halo particles are given in table 4.4.16. The integrated scattering fraction for bremsstrahlung is very small and we don't expect any halo generation from this source. For mott scattering the integrated scattering fraction is comparable to the one obtained in the case of the CLIC drive beam decelerator, but as the superconducting linac of TBONE is a very short accelerator, the halo generation due to beam gas scatteri As the residual gas consists only of H_2 the integrated scattering fraction for bremsstrahlung is very smallng is totally negligible. *Beam Offset*

$S_{\text{mott,tot}}$	3.66×10^{-9}
$S_{\text{brem,tot}}$	3.14×10^{-14}
S_{tot}	3.66×10^{-9}
N_{halo}	1.91

Table 4.4.16: Integrated scattering fraction along the superconducting linac for mott scattering $S_{\text{mott,tot}}$ and bremsstrahlung $S_{\text{brem,tot}}$

Discussion and Analytical Estimates of Halo and Tail Generation Sources not Included in the Simulation

Ionization of the Residual Gas:
The ionization cross section increases with rising beam energy. As the beam energy of TBONE is small we therefore don't expect any significant ionization of residual gas.
Compton Scattering:
The average energy and density of the photons emitted by the surrounding structure decrease with falling temperature. Because the temperature in TBONE is very low (2 K), we can neglect the halo generation due to compton scattering and also the energy spread caused by compton scattering.
Synchrotron Radiation:
The superconducting linac does not include any bending or focusing magnets, where synchrotron radiation could become relevant.
Electron Cloud Effects:
As described in ch. 4.3.4 the electron cloud effect is not relevant in our case as TBONE is a linear electron beam accelerator.
Ion Cloud Effects:
The conventional ion instability only arises in circular accelerators and the fast ion instability normally only in long linear beamlines. In short linear accelerators an occurance of an ion instability is therefore very improbable.
Touschek Effect and Intrabeam Scattering:
If the beam size is very small, beam particles could become halo particles due to Touschek or intrabeam scattering. TBONE is first of all a linear accelerator, where intrabeam scattering has hardly any effect, and in addition a relatively large beam size and therefore both effects are probably negligible.
Space Charge Effect:

Space charge effects are normally only relevant for electron beams with beam energies in the keV range or lower. Therefore we haven't performed any estimates of space charge effects. *Optics Related Effects*

We haven't studied any effects resulting from mismatch, coupling or any dispersive effects, which could be the topic of further studies for TBONE. Nonlinearities are not included either, because only the dipole wakes are simulated and no higher magnetic multipoles are included in the lattice.

Bibliography

[1] K. Wille, *The Physics of Particle Accelerators*.
Oxford University Press, 2000.

[2] T. P. Wangler, *RF Linear Accelerators*.
Wiley-VCH, 2nd ed., 2008.

[3] H. Wiedemann, *Particle Accelerator Physics - Basic Principles and Linear Beam Dynamics*.
Springer Verlag, 1993.

[4] T. C. S. Team, “A 3 tev e^+e^- linear collider based on clic technology,” tech. rep., CERN, 2000.

[5] H. Braun, R. Corsini, J.-P. Delahaye, A. De Roeck, S. Doebert, G. Geschonke, A. Grudiev, C. Hauviller, B. Jeanneret, E. Jensen, T. Lefevre, Y. Papaphilippou, G. Riddone, L. Rinolfi, W.-D. Schlatter, H. Schmickler, D. Schulte, I. Syratchev, M. Taborelli, F. Tecker, R. Toms, S. Weisz, W. Wunsch, and A. Ferrari, “Clic 2008 parameters,” tech. rep., CERN - AB Department, 2008.

[6] D. Proch, *Handbook of Accelerator Physics and Engineering*, ch. 7.3.10, p. 576.
World Scientific Publishing Co. Pte. Ltd, 3 ed., 2006.

[7] A. M. Sessler, “The fel as a power source for a high gradient accelerating structure,” *AIP Conf. Proc. 91*, p. 154, 1982.

[8] L. Rinolfi and T. Kamitani, “The clic positron production scheme,” *LINAC2002*, 2002.

[9] F. Antoniou and Y. Papaphilippou, “Optics design considerations for the clic predamping rings,” *PAC’09*, 2009.

[10] T. E. dAmico, G. Guignard, and T. Raubenheimer, “The clic main linac bunch compressor,” *EPAC’98*, 1998.

[11] D. Schulte, “Emittance preservation in the main linac of clic,” *EPAC’98*, 1998.

[12] E. Adli, *A Study of the Beam Physics in the CLIC Drive Beam Decelerator*.
PhD thesis, University of Oslo, August 2009.

[13] A.-S. Müller, E. Bründemann, S. Casalbuoni, B. Gasharova, M. Havenith, Y.-L. Mathis, A. Plech, and K. Sonnad, “Tbone: Ultra-fast high-power coherent thz to mid-ir radiation facility.” Proposal.

[14] A.-S. Müller, T. Baumbach, E. Bründemann, S. Casalbuoni, B. Gasharova, M. Hagelstein, M. Havenith, S. Hillenbrand, E. Huttel, Y.-L. Mathis, D. A. Moss, A. Plech, R. Rossmanith, and K. Sonnad, “Tbone: Ultra-fast high-power coherent thz to mid-ir radiation facility,” *PAC’09*, 2009.

[15] C. Gerth and F. E. Hannon, “Injector design for the 4gls energy recovery linac prototype,” *EPAC’04*, 2004.

[16] J. Teichert, A. Büchner, P. Evtushenko, F. Gabriel, U. Lehnert, P. Michel, and J. Voigtländer, “Results of beam parameter measurement of the elbe electron accelerator after commissioning,” *Nuclear Instruments and Methods in Physics Research A*, vol. 507, pp. 354–356, 2003.

[17] D. J. Holder, N. Bliss, A. R. Goulden, P. A. McIntosh, and P. L. Smith, “The status of alice, the daresbury energy recovery linac prototype,” *EPAC’08*, 2008.

[18] S. Hillenbrand, “Ein bunch compressor für tbone,” Master’s thesis, Universitt Karlsruhe, October 2009.

[19] “Octave.” http://www.gnu.org/software/octave/.

[20] “The tracking code placet.”

[21] D. Schulte, E. Adli, B. Burkhardt, Helmut Dalena, P. Eliasson, and A. Latina, “The tracking code placet.” Manual.

[22] “The gdfidl electromagnetic field simulator.”

[23] E. D’Amico, G. Guignard, and D. Schulte, “Simulation package based on placet,” *CERN/PS 2001-028 (AE)*, 2001.

[24] “Halo and tail generation package htgen.”

[25] B. Povh, K. Rith, C. Scholz, and F. Zetsche, *Particles and Nuclei*.
Springer, 4 ed., 1999.

[26] H. Bethe and W. Heitler, “On the stopping of fast particles and on the creation of positive electrons,” *Proc. Roy. Soc.A*, vol. 146, p. 83, 1934.

[27] H. Bethe and L. Maximom, “Theory of bremsstrahlung and pair production. i. differential cross section,” *Phys. Rev.*, vol. 93, p. 768, 1954.

[28] H. Olsen, “Outgoing and ingoing waves in final states and bremsstrahlung,” *Phys. Rev.*, vol. 99, p. 1335, 1955.

[29] H. Olsen, L. Maximon, and H. Wergeland, “Theory of high energy bremsstrahlung and pair production in a screened field,” *Phys. Rev.*, vol. 106, p. 27, 1957.

[30] H. Olsen and L. Maximon, “Photon and electron polarization in high-energy bremsstrahlung and pair production with screening,” *Phys. Rev.*, vol. 114, p. 887, 1959.

[31] S. D. Drell and J. Walecka, “Electrodynamic processes with nuclear targets,” *Annals of Physics*, vol. 28, pp. 18–33, 1964.

[32] Y.-S. Tsai, “Pair production and bremsstrahlung of charged leptons,” *Review of Modern Physics*, vol. 46, pp. 815–851, October 1974.

[33] P. D. Group, “Passage of particles through matter,” *Review of Particle Physics*, 2008.

[34] H. W. Koch and J. Motz, “Bremsstrahlung cross-section formulas and related data,” *Review of Modern Physics*, vol. 31, p. 920, October 1959.

[35] S. M. Seltzer and M. J. Berger, “Bremsstrahlungs spectra from electron interactions with screened atomic nuclei and orbital electrons,” *Nucl. Inst. and Meth.*, vol. B12, p. 95, 1985.

[36] H. K. Tseng and R. H. Pratt, “Comments on the calculation of relativistic bremsstrahlung cross sections,” *Phys. Rev. A*, vol. 1, pp. 528–531, Feb 1970.

[37] S. Perkins, D. Cullen, and S. Seltzer, “Eedl,” *UCRL-50400*, vol. 31, 1991.

[38] *Physics Reference Manuel*.
p. 120-134, December 2008.

[39] E. Borie, L. C. Maximon, and H. Olsen, “Molecular coherence effects in radiation processes: Bremsstrahlung,” *Phys. Rev. A*, vol. 2, pp. 1443–1449, Oct 1970.

[40] G. D. Palazzi, “High-energy bremsstrahlung and electron pair production in thin crystals,” *Rev. Mod. Phys.*, vol. 40, pp. 611–631, Jul 1968.

[41] W. Heitler, *The Quantum Theory of Radiation*.
Oxford University Press, 3 ed., 1954.

[42] V. Telnov, “Scattering of electrons on thermal radiation photons in electron-positron storage rings,” *Nuclear Instruments and Methods*, vol. A260, pp. 304–308, 1987.

[43] I. F. Ginzburg, G. L. Kotkin, V. G. Serbo, and V. I. Telnov, “Colliding ge and gg beams based on the single-pass $e^{\pm}e^{-}$ colliders (vlepp type),” *Nuclear Instruments and Methods*, vol. 205, pp. 47–68, 1983.

[44] I. Reichel, *Study of the Transverse Beam Tails at LEP*.
PhD thesis, University of Aachen, 1998.

[45] Y. Baconnier, “Neutralization of accelerator beams by ionization of the residual gas,” *CERN/PS/PSR*, 1984.

[46] M. Inokuti, “Inelastic collisions of fast charged particles with atoms and molecules - the bethe theory revisited,” *Rev. Mod. Phys*, vol. 43, July 1971.

[47] F. F. Rieke and W. Prepejchal, “Cross sections of gaseous atoms and molecules for high-energy electrons and positrons,” *Phys. Rev. A*, vol. 6, October 1972.

[48] G. Rumolo, “Fast ion instability.” Summary.

[49] F. Zimmermann, J. Byrdy, A. Chao, S. Heifets, M. Minty, T. Raubenheimer, J. Seeman, G. Stupakov, and J. Thomson, “Experiments on the fast beam-ion instability at the als,” *SLAC-PUB*, October 1997.

[50] T. Raubenheimer and F. Zimmermann, “Fast beam-ion instability,” *Physical Review E*, vol. 52, pp. 5487–5504, November 1995.

[51] J.-B. Jeanneret, E. Adli, A. Latina, G. Rumolo, D. Schulte, and R. Toms, “Beam dynamics issues in the clic long transfer line,” *EPAC’08*.

[52] T. Raubenheimer, F. Zimmermann, and G. Stupakow, “A fast beam-ion instability,” *PAC95*, 1995.

[53] F. Zimmermann, *Accelerator Physics and Engineering*, ch. Ion Instability, p. 131. World Scientific, 2002.

[54] G. Rumolo and D. Schulte, “Fast ion instability in the clic transfer line and main linac,” *EPAC’08*, 2008.

[55] A. Piwinski, “The touschek effect in strong focusing storage rings,” *DESY*, no. 98-179, 1998.

[56] G. H. Hoffstaetter, M. P. Ehrlichman, and A. B. Temnykh, “Intra beam scattering in linear accelerators, especially erls,” *EPAC’08*, 2008.

[57] M. Fitterer, E. Adli, I. Ahmed, H. Burkhardt, B. Dalena, A. Latina, A.-S. Müller, G. Rumolo, and D. Schulte, “Halo and tail simulations with application to the clic drive beam,” *PAC’09*, 2009.

[58] E. Adli and D. Schulte, “Alignment tolerances for the clic decelerator,” *CLIC-Note-773*, 2008.

[59] J. B. Jeanneret, E. Adli, G. Rumolo, D. Schulte, and R. Tomas, “Beam dynamics issues in the clic long transfer line,” *EPAC’08*, 2008.

[60] A. B. Temnykh, M. P. Ehrlichman, and G. H. Hoffstaetter, “Beam losses due to intra-beam and residual gas scattering for cornell’s energy recovery linac,” *EPAC’08*, 2008.

[61] E. Adli, “Private communication.”

[62] K. L. F. Bane, “Short range dipole wakefields in accelerating structures for the nlc,” *SLAC-PUB*, no. 9663, 2003.

Acknowledgments

Here you have to put your acknowledgements.

Appendix

Appendix A

Basic Waveguide Parameters

For the specification and description of the accelerating and decelerating structures of a LINAC the definition and interpretation of a few characteristic parameters is necessary. Characteristic of accelerating structures in general are discussed in [2].

Quality factor:

The quality factor characterizes the energy losses in the cavity

$$Q = \frac{\text{stored energy per unit length}}{\text{ohmic losses per unit length per radian of the field oscillation}} = \frac{W \cdot \omega_{\mathrm{rf}}}{P} \quad \text{(A.0.1)}$$

where W is the stored energy per unit length, P the ohmic losses per unit length and ω_{rf} the fundamental (accelerating) mode angular frequency.

Shunt-impedance per unit length:

The shunt-impedance per unit length measures the effectiveness of producing an axial electric field for a given power dissipated and is independent of the excitation level of the cavity.

$$Z = \frac{(\text{axial electric field})^2}{\text{ohmic losses per unit length}} = \frac{E^2}{P} \quad \text{(A.0.2)}$$

where E is the axial electric field and P the ohmic losses per unit length.

Appendix B

Scattering Formulas

N is the number of particles per bunch, n_{gas} the particle density in the vacuum, σ the crossection of the process, l the accelerator length.
mean free path length:

$$\lambda_{int} = \frac{1}{n_{\text{gas}}\ \sigma} \tag{B.0.1}$$

scattering probability:

$$P = n_{\text{gas}}\ \sigma \tag{B.0.2}$$

scattering per bunch:

$$P_{\text{bunch}} = P\ N\ l \tag{B.0.3}$$

scattering fraction:

$$S = P\ l \tag{B.0.4}$$

integrated scattering probability:

$$S_{\text{int}} = \sum_{i=1}^{\text{tot. numb. of elements}} P_i\ l_i \tag{B.0.5}$$

Appendix C

Parameter List for the CLIC decelerator and CTF3 TBL

Parameter	Symbol	CTF3	CLIC
DB station length $[\mathrm{m}]$	L	22.4	1053.23
PETS misalignment in x/y $[\mu\mathrm{m}]$			200
Quadrupoles misalignment in x/y $[\mu\mathrm{m}]$			2
number of trains		1	1
Bunches per train	n	1683	2928
Bunch separation $[\mathrm{m}]$	Δz_b	0.025	0.025
number of particles per bunch [10^9]	N	14.6	52.5
initial beam energy $[\mathrm{Gev}]$	E_{initial}	0.15	2.4
final beam energy $[\mathrm{Gev}]$	E_{final}	0.0657746	0.4
initial norm. emittance in x $[\mu\mathrm{m}]$	$\epsilon_{x,\text{initial}}$	150	150.0
initial norm. emittance in y $[\mu\mathrm{m}]$	$\epsilon_{y,\text{initial}}$	150	150.0
final norm. emittance in x $[\mu\mathrm{m}]$	$\epsilon_{x,\text{final}}$	199.458	351.4
final norm. emittance in y $[\mu\mathrm{m}]$	$\epsilon_{y,\text{final}}$	203.764	340.0
initial β-function in x $[\mathrm{m}]$	$\beta_{x,\text{initial}}$	0.827315	0.579
initial β-function in y $[\mathrm{m}]$	$\beta_{y,\text{initial}}$	4.72172	3.354
final β-function in x $[\mathrm{m}]$	$\beta_{x,\text{final}}$	1.59991	5.029
final β-function in y $[\mathrm{m}]$	$\beta_{y,\text{final}}$	4.724	6.778
initial rms beam size in x $[\mathrm{mm}]$	$\sigma_{x,\text{initial}}$	0.6502	0.14
initial rms beam size in y $[\mathrm{mm}]$	$\sigma_{y,\text{initial}}$	1.553	0.33
final rms beam size in x $[\mathrm{mm}]$	$\sigma_{x,\text{final}}$	1.575	1.50
final rms beam size in y $[\mathrm{mm}]$	$\sigma_{y,\text{final}}$	2.735	1.71
initial beam divergence in x' $[\mathrm{mrad}]$	$\sigma_{x',\text{initial}}$		0.23
initial beam divergence in y' $[\mathrm{mrad}]$	$\sigma_{y',\text{initial}}$		0.10
final beam divergence in x' $[\mathrm{mrad}]$	$\sigma_{x',\text{final}}$		0.30
final beam divergence in y' $[\mathrm{mrad}]$	$\sigma_{y',\text{final}}$		0.25

Table C.0.1: Beam Parameters of the CLIC and CTF3 TBL Drive Beam

Parameter	Symbol	CTF3	CLIC
pressure [nTorr]	p	10	10
temperature [K]	T	300	300
molecule density [m^{-3}]	n_{gas}	$3.22 \cdot 10^{14}$	3.22×10^{14}
photon density [m^{-3}]	n_p	$5.45 \cdot 10^{14}$	5.45×10^{14}
average photon energy [eV]	$\langle\epsilon\rangle$	0.07	0.07

Table C.0.2: CLIC/CTF3 vacuum specifications